Correlation models of critical heat flux and associated temperature for spray evaporative cooling of vibrating surfaces

Article (Published Version)

International Journal of Heat and Mass Transfer 179 (2021) 121735

Contents lists available at ScienceDirect

International Journal of Heat and Mass Transfer

journal homepage: www.elsevier.com/locate/hmt

Correlation models of critical heat flux and associated temperature for spray evaporative cooling of vibrating surfaces

Alireza Sarmadian, J.F. Dunne*, J. Thalackottore Jose, C.A. Long, J-P Pirault

Department of Engineering and Design, School of Engineering and Informatics, University of Sussex, Falmer, Brighton, BN1 9QT, UK.

ARTICLE INFO

Article history:
Received 27 March 2021
Revised 21 June 2021
Accepted 12 July 2021

ABSTRACT

Prediction models have been constructed to investigate the effect of vibrating surfaces on the critical heat flux (CHF) and its associated temperature in spray evaporative cooling. Dimensional analysis has been used to construct the models to account for the influence of key dynamic parameters. Experimental measurements have been obtained from a flat, electrically-heated, copper test-piece, located inside a spray-chamber mounted on top of a shaker. A wide range of large-amplitude and high-frequency measurements have been obtained which correspond to test conditions for a piece of hardware mounted on board a light-duty automotive vehicle with vibration amplitudes ranging from 0 to 8 mm and frequencies from 0 to 200 Hz. Three nozzle types have been fed with distilled water at flow rates ranging from 55 to 100 ml/min being used to cool with subcooling degrees ΔT_{sub} ranging from 10°C to 45°C. Measured data for both static and dynamic cases have been used to explore the influence on the CHF and the surface-to-fluid saturation temperature at which this occurs, of subcooling degrees, surface vibration amplitude and frequency, vibrational Reynolds Number and vibrational Acceleration Number. The measured data has also subsequently been used to calibrate the predictive models for use in thermal management systems. Static measurements (without vibration) show that the influence of flow rate, volumetric flux, and subcooling are largely in agreement with published literature. For dynamic cases, the influence of vibration is best explained in terms of the nondimensional parameters: Vibration Reynolds Number and Acceleration Number. The effect of vibration on CHF and associated temperature is assessed in detail for the three nozzle types at different flow rates and degrees of subcooling. Predictions of CHF and associated excess temperature, using the calibrated correlation models for the dynamic conditions, are very reasonable, and suitable for the intended purpose of ensuring safe operation of thermal management systems using spray evaporative cooling.

1. Introduction

Spray cooling is receiving considerable attention for advanced thermal management systems. The reason is that spray heat transfer characteristics are especially good in terms of achieving high Coefficient of Performance (COP) [1], high-heat flux, and high-temperature heat removal [2]. Spray cooling applications can be found in numerous areas. In the automotive sector for example, they include both battery electric [3], and hybrid electric vehicles [4]. In power electronics they include high-power LEDs [4], IGBTs [5] and associated IGBT heat sinks [6]. In aerospace, spray cooling applications are found in micro-electro-mechanical systems [7], and high performance lithium-ion batteries [8,9]. And in power generation, for thermal management of superheaters [10], hydrogen-based systems [11], storage tanks [12], and surface temperature control of hydrogen fuel cell catalysts [13]. Elsewhere, in carbon capture, water spray cooling for the CO_2 separation proves most cost-effective for gasifier design [14]. These applications conform to the UK government 10-point green industrial revolution plan [15]. But with the goal of achieving net zero carbon emissions by 2050, increasingly efficient and safe thermal management systems will be essential. Spray *evaporative* cooling has a role to play in achieving that goal because it offers even better characteristics than single-phase spray cooling.

In general, thermal management systems require two attributes: efficacy and safety. For evaporative spray cooling, efficacy requires a thorough understanding of the dynamic and heat transfer mechanisms involved. Spray dynamics involve many com-

* Corresponding author.
E-mail addresses: A.Sarmadian@sussex.ac.uk (A. Sarmadian), j.f.dunne@sussex.ac.uk (J.F. Dunne).

https://doi.org/10.1016/j.ijheatmasstransfer.2021.121735

Nomenclature

$\dot{m}$	mass flow rate (kg/s)
ν''	volumetric spray flux (m^3s^{-1}/m^2)
$\bar{\nu}''$	average volumetric spray flux (m^3s^{-1}/m^2)
A	surface area (m^2)
Ac	dimensionless acceleration (units of g)
a	Amplitude of vibration (m)
Bo	Boiling number (-)
C_p	specific heat (kJ/kg k)
d	diameter(mm)
d_{05}	mass or volume median diameter (m)
d_{32}	Sauter mean diameter (m)
f	Frequency (Hz)
G	mass velocity (kg/m^2s)
h	specific enthalpy (kJ/kg)
H	height (m)
Ja	Jacob number
k	thermal conductivity (W/m K)
L	length (mm)
P	pressure (kPa)
Pr	Prandtl number, $C_p\mu/k$
v	volumetric flow rate (m^3/s) or (l/h)
q	heat flux (kW/m^2)
Re	Reynolds number
R_t	mean roughness height (μm)
T	temperature (K)
u	velocity
We	Weber number

Greek symbols

μ	dynamic viscosity (Kg/m s)
Δp	pressure drop (kPa)
α	spray angle
ρ	density (kg/m^3)
σ	surface tension (N/m)
ω	Angular velocity (Hz)
δ	liquid film thickness (m)

Subscripts

am	ambient
at	atmospheric
ch	chamber
CHF	Critical Heat Flux
c	coolant
d	droplet
f	liquid phase
v	vapor phase
V	vibration
g	gas side
h	heater
H	heater surface
i	inner
l	liquid
lat	latent
o	orifice
ref	refrigerant
s	surface
sat	saturation
sub	subcooling
w	Wall

plex relations, from droplet impingement to rebound and splashing, followed by bubble generation during nucleation within the liquid film [16]. Various complexities are evident such as impinged drop convection, liquid film evaporation, film-flow convection, surface and secondary nucleate boiling [17]. To better understand how these mechanisms combine, researchers have separated different regimes of spray cooling based on achievable excess (or 'superheat') temperature and heat flux (where the excess temperature is the difference between the cooled surface temperature and the fluid saturation temperature) [2]. Spray cooling regimes start from single-phase (similar to pool boiling), with high degrees of subcooling appropriate for low heat-flux and low-temperature requirements. The next regime is nucleate boiling with high heat transfer rates and high surface temperature capabilities ideal for cooling systems with extreme thermal requirements [19]. Following the so called 'critical heat flux', transition boiling occurs. In the transition boiling regime, bubbles merge forming small slugs in the liquid film resulting in partial contact of a thin surface layer. The Leidenfrost point of minimum heat flux occurs when the heat transfer mode changes from transition boiling to film boiling, where a thermally-insulated layer forms between the hot surface and the impinging spray droplets. Film boiling therefore gives poor heat transfer. Focusing specifically on the heat transfer mechanism associated with the nucleate boiling regime, for nonvibrating surfaces, the momentum of the liquid spray (emerging from a 'pressure' nozzle) is known to be sufficiently high to cause break-up of the liquid into fine droplets [2]. These droplets impinge onto the hot surface resulting in bubble nucleation within a liquid film. High heat flux is achievable because high velocity droplets are able to penetrate the vapour barrier created by boil-off'. Compared with static surfaces, there are however significant differences in the heat flux for vibrating surfaces as a function of excess temperature. The precise heat transfer mechanisms associated with spray evaporative cooling of vibrating surfaces are not yet fully understood.

The published literature on spray cooling thermal management systems, classifies the spray flow field as either 'variable' or 'intermittent'. Variable flow spray cooling systems need pump speed control. The intermittent class (also known as pulsed-flow spray cooling) requires control of solenoid valves mounted just before a nozzle [19]. Intermittent spray cooling compared with continuous spray cooling experimental results, offers liquid savings of 10 – 90% for the same energy efficiencies [20]. In fact, a recent publication [21], gives comparisons between intermittent (pulsate) and continuous spray, in terms of the specific heat flux (heat dissipated per kilogram of water). Enhancements of more than 100% are reported.

Wang et al. [5] examined control systems in order to evaluate a spray cooling system on sintered porous wick made from copper. To keep the system within a safe working temperature, fuzzy logic and PID controllers were implemented. It was reported that the performance of a Fuzzy-PID controller was superior to PID because it responded faster with a smaller error. Ding et al. [6] used a PID controller to keep the Insulated-Gate-Bipolar-Transistor (IGBT) junction temperature below 150 °C for safe operation. A spray cooling system (working with water) was used for cooling. The results illustrate that the Fuzzy-PID is better than conventional PID for controlling junction temperatures. Sai and Reddy [10] developed a controller to regulate the temperature of superheated steam in a power plant. Water was considered as the working fluid in the spray cooling system. To control the temperature, a fuzzy gain scheduler and conventional PID were implemented. The results showed that the settling time and oscillations associated with peak overshoot of the PID controller, were higher. By contrast, the fuzzy gain scheduler was capable of eliminating the oscillations and reducing the time needed for settling.

To enhance the cooling performance, significant attention has been paid to intermittent spray cooling systems. Continuous systems use relatively large volumes of coolant. To reduce the volume of coolant, solenoid valves have been used to control two factors: i) duty cycle (defined as the percentage of cycle time associated

with injecting liquid), and ii) spray frequency. When both factors are controlled, taking account of heat load, it is possible to increase cooling efficiency. Panao and Moreira [21] studied pulsed-spray impinging onto hot surfaces. Tests were undertaken to demonstrate the impact of injection parameters including frequency, duration, and pressure on the cooling performance. The test conditions, similar to applications in hybrid EV configurations, were considered. It was observed by the experiments that increasing the injection pressure results in decreasing heat flux. The data also suggested that for the range of injection conditions for real engines, time variations of the transferred heat is more dependent on the coolant mass velocity than on the size and axial velocity of the droplets.

In another study, by Moreira and Panao [22], and Moreira and Panao [23], it was demonstrated that increasing the frequency within the range of 10 to 20 Hz, gives rise to an increase in the rate of local transferred heat. However, it was also observed that by further increasing frequency, the heat transfer rate declines. Panao and Moreira [24] also investigated a two-phase flow cooling system using several intermittent sprays. Spray characteristics, i.e. the size of droplets, and their axial velocity, and the thermal features of the surface, were considered to explain the factors which have high impact on heat transfer. As a result, it was reported that injection frequency, and the temperature of the surface, have greatest effect on the amount of transferred heat, not the spray features prior to impact. Moreira et al. [25] assessed an intermittent spray cooling system and found that under conditions of 5 ms pulse duration at the critical heat flux, for smaller injection frequency, cooling efficiency increases. Panao and Moreira [26] suggested an intermittent spray cooling system for thermal management purposes and investigated the influences of different parameters such as injection frequency, pressure, and pulse duration. The results demonstrated that injection frequencies do not significantly affect the spray characteristics. A 'duty cycle' parameter was introduced, defined as the percentage of cycle time associated with injecting liquid. Small duty cycles were found to be effective in controlling the surface temperature. Also, higher performance was obtained when injection pressure was lower. A comparison between the performance of continuous and intermittent spray cooling showed that by using the intermittent mode, a significant reduction in coolant use is observed for similar cooling efficiency. And in a study by Panao et al. [27], it was concluded that the heat transfer rates increase when the period is shorter between the consecutive injection cycles. Somasundaram and Tay [28] studied spray cooling systems in continuous and intermittent conditions to reveal the influence of heat flux and mass velocity on fluctuations in the surface temperature and other parameters. Their experiments showed that when the temperature of the surfaces is sufficiently superheated, fluctuations are reduced. In a different investigation on intermittent cooling systems by Majaron et al. [29], it was observed that cooling rates increase when the duty cycle was neither high nor low. But with short cycles, a significant decrease in the rates of heat removal was observed.

For design of safe thermal management systems, the prediction of critical heat flux immediately after nucleate boiling plays an important role because two-phase spray is the desired mode. Remaining within this regime requires accurate prediction of the transition to CHF. Mudawar and Valentine [30] reported that prediction of steady-state temperature is difficult in the transition to film boiling which occurs just after the CHF point (caused by low heat flux and surface oxidation). This means to achieve robust temperature control in a thermal management system, models are required to predict both the critical heat flux and the excess temperature at which CHF occurs. Owing to the complexity of these heat transfer mechanisms, and the need for efficient prediction of CHF, zero dimensional models are often adopted. These models, and their range of valid operation, are listed in Table 1. Owing to uncertainty in measured data, and in the model fitting process, error analysis in both phases of thermal management and controller design, is important. But predictive models of the excess temperature at which CHF occurs are rare, stemming mainly from contradictory issues associated with the dynamics of the heat transfer mechanisms, and the key parameters. Examples include the empirical surface temperature models at CHF by Mudawar and Valentine [30] and Dou et al. [31], also the analytical model for aerospace applications by Baysinger et al. [32]. But to include dynamic effects such as vibration, more experimental evidence is needed.

The literature shows that vibration affects heat transfer involving Newtonian and non-Newtonian fluids, and nano-fluids [33]. Vibration velocity and acceleration are important parameters and need to be considered in systems exposed to dynamic agitation such as automotive vehicles [34] and aircraft [35,36]. The effects of vibration on spray cooling in single-phase [37], incipient boiling [38,39], and nucleate boiling [40] modes have recently been investigated. Reynolds number and nondimensional Acceleration Number have been used to address the effects of vibration with a reliance on either empirical or theoretical modelling. The Vibrational Reynolds Number is a representation of the turbulence caused by vibrating surfaces [41]. It can be used in modelling to establish how vibration induced turbulence affects the heat transfer. The Acceleration Number can explain the effects of experimentally-measured acceleration on spray cooling heat transfer. Elston et al. [42,43] studied the effect of acceleration on the cooling performance of spray arrays on NASA's C-9 aircraft exposed to acceleration levels from 0.02g to 2.02g, reporting that acceleration impedes spray heat transfer in nucleate boiling. By contrast, Michalak et al. [44] claimed that accelerations between 0.15g and 1.8g, increasingly enhances spray heat transfer. There are however no studies published examining the effect of vibration on CHF, and how it influences the corresponding CHF excess temperature - a fact that makes this study novel.

The objective of this paper is to reveal the influences of vibration on CHF and excess temperature for parameters relevant to the road transport sector. Correlation models of CHF and corresponding excess temperature are developed and calibrated. These empirical correlations can be used for design of spray evaporative cooling systems and in their subsequent thermal management. Construction of correlation models is first described, followed by a detailed examination of the effects of vibration on CHF and excess temperature, culminating in the calibration of correlation models to provide a predictive capability for the observed physics.

2. A correlation modelling approach for CHF and corresponding temperature predictions

This section outlines a modelling approach to obtain CHF and excess temperature both with, and without vibration. This is based on dimensional analysis [45] in the form of the generalized Π-Theorem proposed by Sonin [46] - a developed form of the well-known Buckingham Π-Theorem [47,48]. The method has been widely used in developing the empirical correlations, in particular, for spray cooling. For prediction of critical heat flux q_{CHF} with static surfaces, it can be established from Table 2, that the heat flux, as a dependent variable, can be completely determined from the fluid properties, geometry, forcing, and spray specifications as provided in the functional relationship according to:

$$q_{Static-CHF} = \varphi\big(\rho_l,\ \rho_v,\ h_{fg}, \mu_l, Cl, \sigma, T_c, P_n, P_{ch}, \Delta T_{sub}, P_{at}, u_d, \text{ or } u_m, \dot{m}], \text{or } \nu \text{ or } \bar{v}'',\ d_{32} \text{ or } d_{05}, H\big) \quad (1)$$

where the dimensions and description of the different parameters are given in Table 2.

For vibrating surfaces producing a dynamic-CHF, there are no published studies which have employed dimensional analysis.

Table 1
Studies on the prediction of Critical Heat Flux (CHF).

Authors	Working fluid	Test conditions: (as reported in referenced publication)	Error range of the correlations (%)	Experimental uncertainty of measured heat flux (%)	Derived experimental correlations*
Mudawar and Valentine (1989) [30]	**Water**	$T_c = 23 - 80$°C, $\nu'' = 0.6 \times 10^{-3} - 9.96 \times 10^{-3} m^3 s^{-1}/m^2$ $d_{0.5} = 0.434$-2.005 mm, u_m =10.6-26.5 m/s	±20	-	(C1)
Estes and Mudawar (1995) [49]	**Water, FC-72, FC87**	$\nu = 2.52 \times 10^{-6} - 3.15 \times 10^{-5}\ m^3 s^{-1}$, $\Delta T_{sub} = 13 - 33$°C	±25	-	(C2)
Mudawar and Estes (1995) [50]	**FC-72, FC87**	$\nu'' = 16.6 \times 10^{-3} - 216 \times 10^{-3} m^3 s^{-1}/m^2$, $\Delta T_{sub} = 13 - 33$°C	±30	-	(C3)
Sehmbey et al. (1995) [51]	**Liquid nitrogen Water**	$d_{32} = 14 - 29\ \mu m$, $G = 16.9 - 88.9$ kg/m^{2}s, $P_n = 2.8 - 8.3\ bar$	±30	±8	(C4)
Chow et al. (1996) [52]	**Liquid nitrogen Air-water R-113**	$\Delta T_{sub} = 0 - 50$°C, $u_m = 10 - 50\ m/s$, $G = 1.12 - 6.75$ kg/m^{2}s	±30	-	(C5)
Sawyer et al. (1996) [53]	**Water**	$u_m = 2.4 - 4.6\ m/s$, $We = 175 - 730$	±22	±5	(C6)
Cabrera and Gonzalez (2003) [54]	**Water**	$\Delta T_{sub} = 25 - 78$°C, $P_n = 1 - 1.8\ bar$, $R_t = 5 - 79 \mu m$, $G = 340 - 750$ kg/m^{2}s	±15	±10	(C7)
Jian and Dhir (2004) [55]	**Water**	$\nu'' = 2.9 \times 10^{-3} - 5.1 \times 10^{-3} m^3 s^{-1}/m^2$, $T_c = 23 - 70$°C	±23	±4.3	(C8)
Silk et al. (2007) [56]	**Water Methanol Perfluorocarbons**	$Pr = 0.33$, $T_{sat} = 31 - 80$°C	±30	-	(C9)
Visaria and Mudawar (2008) [57]	**FC-77**	$\Delta T_{sub} = 22 - 70$°C, $\nu = 3.33 - 20.4\ cm^3 s^{-1}$	±30	-	(C10)
Abbasi and Kim (2011) [58]	**PF-5060**	$\Delta T_{sub} = 11 - 31$°C, $P_n = 2 - 6.9\ bar$, $H = 3,\ 5,$ and 7mm	±25	±6.3	(C11)
Thiagarajan et al.(2013) [59]	**HFE-7100**	$\nu = 1.1 \times 10^{-6} - 15.8 \times 10^{-6}\ m^3 s^{-1}$, $\Delta T_{sub} = 0 - 30$°C	±30	±6	(C12)
Thiagarajan et al. (2013) [59]	**HFE-7100**	A microporous surface: $100 \mu m$ coating, porosity of 57%.	±30	±6	(C13)
Dou et al. (2015) [31]	**Water**	$G = 6.2 - 12.4$ kg/m^{2}s, $\Delta P = 2 - 7 bar$	±20	±6.3	(C14)
Zhao et al. (2019) [60]	**Water**	$\Delta T_{sub} = 61.3$°C, $\bar{\nu}'' = 2.42 - 8.04$ m^{3}s^{-1}/m^2	±12.31	±4.6	(C15)
$q_{CHF} = 122.4 \rho_g h_{fg} \nu'' [1 + 0.0118 (\frac{\rho_g}{\rho_f})^{1/4} (\frac{\rho_f C_{p,f} \Delta T_{sub}}{\rho_g h_{fg}})] (\frac{\sigma}{\rho_f \nu''^2 d_{32}})^{0.198}$					(C1)
$q_{CHF} = 134.3 \rho_g h_{fg} \nu'' [1 + 0.0118 (\frac{\rho_g}{\rho_f})^{1/4} (\frac{\rho_f C_{p,f} \Delta T_{sub}}{\rho_g h_{fg}})] (\frac{\sigma}{\rho_f \nu''^2 d_{0.5}})^{0.192}$ (C1)					
$q_{CHF,p} = 2.3 \rho_g h_{fg} \nu'' (\frac{\rho_f}{\rho_g})^{0.3} (\frac{\rho_f \nu''^2 d_{32}}{\sigma})^{-0.35} [1 + 0.0019 (\frac{\rho_f C_{p,f} \Delta T_{sub}}{\rho_g h_{fg}})]$					(C2-a)
$q_{CHF,p} = \frac{q_{CHF} L^2}{L^2 (\pi/4)} = \frac{4}{\pi} q_{CHF}$					(C2-b)
$\nu'' = \frac{2\nu}{\pi L^2} [(1 + \cos(\frac{\theta}{2})) \cos(\frac{\theta}{2})]$					(C2-c)
$q_{CHF} = 1.467 \rho_g h_{fg} \bar{\nu}'' [(1 + \cos(\frac{\theta}{2})) \cos(\frac{\theta}{2})]^{0.3} (\frac{\rho_f}{\rho_g})^{0.3} [\frac{\rho_f \bar{\nu}''^2 d_{32}}{\sigma}]^{-0.35} [1 + 0.0019 (\frac{\rho_f C_{p,f} \Delta T_{sub}}{\rho_g h_{fg}})]$					(C3)
$q_{CHF} = 0.31 \rho_g h_{fg} (\frac{\rho_f}{\rho_g})^{0.5} (\frac{6 \bar{\nu}'' \sigma}{\pi \rho_f d_{32}})^{1/3}$					(C4)
$q_{CHF} = 0.38 \rho_g h_{fg} u_m (\frac{\rho_f u_m^2 d_{32}}{\sigma})^{-1/3} (\frac{\rho_f}{\rho_g})^{-0.5} (\frac{P_d}{P_s})^{-0.25}$					(C5)
$q_{CHF} = 0.166 \rho_f h_{fg} u_d (\frac{\rho_f u_d^2 d_d}{\sigma})^{-0.4138} (\frac{f d_d}{u_d})^{0.8906}$					(C6)
$q_{CHF} = 1.623 (We)^{-0.315} (S_t)^{0.0465} = 1.623 G h_{fg} (\frac{\rho_f u_d^2 d_d}{\sigma})^{-0.315} (\frac{R_t}{R_d^+})^{0.0465}$					(C7)
$q_{CHF} = 2.3 \rho_g h_{fg} \bar{\nu}'' (\frac{\rho_f}{\rho_g})^{0.5} (\frac{\rho_f \bar{\nu}''^2 d_o}{\sigma})^{-0.2} [1 + 0.0019 (\frac{\rho_f C_{p,f} \Delta T_{sub}}{\rho_g h_{fg}})]$					(C8)
$q_{CHF} = 5.3 Re_d^{0.55} Pr_f^{0.33} [\frac{1 + 0.8 (C_{p,f} \Delta T_{sub}/h_{fg})}{(\frac{\rho_f}{\rho_g})^{0.4}}] (\frac{\pi N^+ d_{32}^3}{6})^{0.09} (\frac{k_f}{L}) (\frac{h_{fg}}{c_{p,f}})$					(C9)
$q_{CHF,p} = 2.3 \rho_g h_{fg} \nu'' (\frac{\rho_f}{\rho_g})^{0.3} (\frac{\rho_f \nu''^2 d_{32}}{\sigma})^{-0.35} [1 + 0.005 (\frac{\rho_f C_{p,f} \Delta T_{sub}}{\rho_g h_{fg}})]$					(C10)
$q''_{CHF} = 9.15 * 10^4 P^{0.4} (1 + 2.42 (\frac{C_{p,f} \Delta T_{sub}}{h_{fg}}))^{0.52}$					(C11)
$q_{CHF} = 1.449\ \rho_g h_{fg} \bar{\nu}'' (\frac{\rho_f}{\rho_g})^{0.3} [\frac{\rho_f \bar{\nu}''^2 d_{32}}{\sigma}]^{-0.3371} [1 + 0.0058 (\frac{\rho_f C_{p,f} \Delta T_{sub}}{\rho_g h_{fg}})]$					(C12)
$q_{CHF} = 2.14 \rho_g h_{fg} \bar{\nu}'' (\frac{\rho_f}{\rho_g})^{0.3} [\frac{\rho_f \bar{\nu}''^2 d_{32}}{\sigma}]^{-0.363} [1 + 0.0058 (\frac{\rho_f C_{p,f} \Delta T_{sub}}{\rho_g h_{fg}})]$					(C13)
$q_{CHF,p} = 2.52 \times 10^{-3} \rho_g h_{fg} \nu'' (\frac{\rho_f \bar{\nu}''^2 d_{32}}{\sigma})^{-0.4255} [1 + 0.013 (\frac{\rho_f}{\rho_g})^{-0.25} (\frac{\rho_f C_{p,f} \Delta T_{sub}}{\rho_g h_{fg}})]$					(C14)
$q_{CHF} = 58.0628 \rho_g h_{fg} \bar{\nu}'' [1 + 0.00118 (\frac{\rho_f}{\rho_g})^{-0.25} (\frac{\rho_f C_{p,f} \Delta T_{sub}}{\rho_g h_{fg}})] We^{-0.2054} St^{0.4462}$					(C15)

* Developed correlations associated with Refs. [30,49–59,31,60] identified by Equations C1 to C15 as appropriate:

Table 2
Parameters with dimensions in SI and MLT systems.

Quantity	Symbol	Dimensions	
		SI	MLT
q_{ch}	Heat Flux	W/m^2	MT^{-3}
ρ_1	Density	kg/m^3	ML^{-3}
h_{fg}	Latent heat	J/kg	L^{2}T^{-2}
μ	Dynamic viscosity	Kg/m s	ML^{-1}T^{-1}
C_l	Specific heat	J/kg k	L^{2}T$^{-2}\theta^{-1}$
σ	Surface tension	N/m	MT^{-2}
T	Coolant temperature	K	θ
P_2	Pressure	Pa	ML^{-1}T^{-2}
ΔT_{sub}	Subcooling degree	K	θ
u_3	velocity (u_d and $u_m^2 = \frac{2\Delta P}{\rho}$ based on [64])	m/s	LT^{-1}
$\dot{m}$	Mass flow rate	kg/s	MT^{-1}
v	Volumetric flow rate	m^3/s	L^3 T^{-1}
$\bar{v}''$	Average volumetric spray flux	m^{3}s^{-1}/m^2	LT^{-1}
d_{32}	Sauter mean diameter (correlated in [65])	m	L
d_{05}	mass or volume median diameter (correlated in [66])	m	L
d_H	Hydraulic diameter of the heating surface	m	L
H	Nozzle to surface distance	m	L
a	Amplitude	m	L
ω	Angular frequency	1/s	T^{-1}
g	Acceleration of gravity	m/s^2	LT^{-2}

[1]subscripts v and l are respectively vapour and liquid phases.
[2]subscripts n, ch, and at represent nozzle, chamber, and atmosphere, respectively.
[3]subscripts d and m are respectively droplet and mean droplet breakup velocities.
For model fitting, heat flux, latent heat, specific heat, and pressure, are respectively in kW/m^2, kJ/kg, kJ/kg k, and kPa.

Therefore, there is no correlation available to predict critical heat flux (See Table 1). To develop a functional relationship, fluid dynamics suggests that the heat flux should depend not only on the static condition parameters but also the vibration amplitude (a) and angular frequency ($\omega = 2\pi f$). To achieve this, the proposed functional form is:

$$q_{Dynamic-CHF} = \varphi\big(\rho_l,\ \rho_v,\ h_{fg}, \mu_l, C_l, \sigma, T_c, P_n, P_{ch}, \Delta T_{sub},\ P_{at}, u_d \text{ or } u_m, \dot{m} \text{ or } v \text{ or } \bar{v}'',\ d_{32} \text{ or } d_{05}, d_H, H, a, \omega, g\big) \quad (2)$$

where d_H is the hydraulic diameter of the heating surface, and g is gravitational acceleration, and where the dimensions and description of the parameters are given in Table 2. After defining independent variables (key parameters) through dimensional analysis, using the generalized Π-Theorem, invariant parameters for different cases can be identified. Invariant parameters (such as Chamber Pressure) can be identified in the test procedure. For example, when experiments are only undertaken at atmospheric pressure, then those dimensionless Π-parameters that comprise entirely invariant quantities, can be neglected, which results in simplification. All the derived functional forms corresponding to the different test plans for both dynamic and static conditions are provided in Table 3.

Based on invariant parameters, three different test procedures are considered, either for static or dynamic environments: i) with variable pressure, and degree of subcooling is indicated as '*None*' for 'Invariant Parameter' in Table 3; ii) under constant pressure (with invariant P_{ch} in the second column of Table 3); and iii) constant pressure and degrees of subcooling (P_{ch}, ΔT_{sub}). In this study, the functional forms with invariant P_{ch} are used. And as provided on the third column of table 3, the number of Π-terms correspond to those for fixed P_{ch} and ΔT_{sub} which is resulted by Generalized Π–Theorem algorithm.

Dimensionless functional forms can be derived based on model requirements. Here '*spray specifications*' and '*flow rate*' are relevant (as in the fourth column of Table 3). Whether, this is for design purposes (in which spray specifications are important), or for a special control approach (where the pumping flow rate plays an important role on the wall temperature control) different dimensionless Π–terms can be obtained (as in the last column of Table 3). Also shown in Table 3, are three dimensionless numbers (common in spray fluid mechanics). These are Boiling Number ($Bo = \frac{qH}{\mu_l h_{fg}}$), Jacob Number ($Ja = \frac{C_l \Delta T_{sub}}{h_{fg}}$), and Weber Number ($We = \frac{\rho_l (u_m^2 or \bar{v}''^2) d_{32}}{\sigma}$). Owing to the high dependency of CHF on the 'subcooling' temperature, $\Delta T_{sub} = T_{sat} - T_c$ is used in Jacob number. In the functional forms corresponding to '*flow rate*' measurements, $\frac{\rho_l \sigma \dot{m}}{{\mu_l}^3}$ is substituted for Weber number, which has spray specifications of u_m *or* $\bar{v}''$ and d_{32}. For functional forms with invariant parameters of P_{ch} and ΔT_{sub}, the Jacob number $Ja = \frac{C_l \Delta T_{sub}}{h_{fg}}$ also stays invariant and therefore is eliminated according to the Generalized Π–Theorem. For dynamic conditions, the Vibrational Reynolds Number $Re_V = \frac{\rho_l a \omega d_H}{\mu_l}$, and the dimensionless Acceleration Number $\frac{\omega^2 a}{g}$ have also been derived.

The Functional forms should also be chosen to take measurement factors into consideration (i.e. which sensors are being used for system identification, and subsequently for the thermal management. There are however conflicting findings as pointed out by Liang et al. [18], in respect of spray effects on the CHF, and Chen et al. [61] who found that CHF is independent of Sauter mean diameter. Furthermore, the use of mean droplet velocity is not recommended for correlating CHF data [49] owing to its failure to account for the cumulative effect of multi-droplet impact. A view supported by Toda [62,63], who showed that for mist cooling, CHF for water sprays is insensitive to droplet velocity. For this reason, for the purposes of gaining an understanding on the dependence of CHF on key parameters, and subsequently for thermal management, the CHF modelling approach adopted here, makes use of functional forms involving '*flow rate*' for both static and dynamic cases as follows:

$$Bo = a\, Ja^{b} \left(\frac{\rho_l^2 \sigma v}{{\mu_l}^3}\right)^{c} \text{(Static)} \quad (3)$$

$$Bo = a\, Ja^{b} \left(\frac{\rho_l^2 \sigma v}{{\mu_l}^3}\right)^{c} Re_V^{d} \left(\frac{a}{H}\right)^{e} Ac^{f} \text{(Dynamic)} \quad (4)$$

where $Ac = \frac{\omega^2 a}{g}$ is the dimensionless Acceleration Number, and where a, b, c, d, e, and f are correlation parameters.

Table 3
Dimensional analysis for CHF prediction.

Surface condition	Invariant Parameter	Number of Π-terms	Measurements needed	Functional form
Static (No vibration)	None	4	Spray spec.[3]	$\frac{qH}{\mu_l h_{fg}} = f(\frac{C_l \Delta T_{sub}}{h_{fg}}, \frac{\rho_l (u_m^2 \text{or} \bar{v}'^2) d_{32}}{\sigma}, \frac{P_{ch}}{P_{at}}, \frac{\rho_l}{\rho_v})$
			Flow rate	$\frac{qH}{\mu_l h_{fg}} = f(\frac{C_l \Delta T_{sub}}{h_{fg}}, \frac{\rho_l \sigma \dot{m}}{\mu_l^3} \text{or} \frac{\rho_l^2 \sigma v}{\mu_l^3}, \frac{P_{ch}}{P_{at}}, \frac{\rho_l}{\rho_v})$
	P_{ch}	2	Spray spec.	$\frac{qH}{\mu_l h_{fg}} = f(\frac{C_l \Delta T_{sub}}{h_{fg}}, \frac{\rho_l (u_m^2 \text{or} \bar{v}'^2) d_{32}}{\sigma})$
			Flow rate	$\frac{qH}{\mu_l h_{fg}} = f(\frac{C_l \Delta T_{sub}}{h_{fg}}, \frac{\rho_l \sigma \dot{m}}{\mu_l^3} \text{or} \frac{\rho_l^2 \sigma v}{\mu_l^3})$
	P_{ch}, ΔT_{sub}	1	Spray spec.	$\frac{qH}{\mu_l h_{fg}} = f(\frac{\rho_l (u_m^2 \text{or} \bar{v}'^2) d_{32}}{\sigma})$
			Flow rate	$\frac{qH}{\mu_l h_{fg}} = f(\frac{\rho_l \sigma \dot{m}}{\mu_l^3} \text{or} \frac{\rho_l^2 \sigma v}{\mu_l^3})$
Dynamic (Vibration)	None	7	Spray spec.	$\frac{qH}{\mu_l h_{fg}} = f(\frac{C_l \Delta T_{sub}}{h_{fg}}, \frac{\rho_l (u_m^2 \text{or} \bar{v}'^2) d_{32}}{\sigma}, \frac{P_{ch}}{P_{at}}, \frac{\rho_l}{\rho_v}, \frac{a}{H}, \frac{\omega^2 a}{g}, \frac{\omega a}{u_d})$
			Flow rate	$\frac{qH}{\mu_l h_{fg}} = f(\frac{C_l \Delta T_{sub}}{h_{fg}}, \frac{\rho_l \sigma \dot{m}}{\mu_l^3} \text{or} \frac{\rho_l^2 \sigma v}{\mu_l^3}, \frac{\rho_l a \omega d_H}{\mu_l}, \frac{P_{ch}}{P_{at}}, \frac{\rho_l}{\rho_v}, \frac{a}{H}, \frac{\omega^2 a}{g})$
	P_{ch}	5	Spray spec.	$\frac{qH}{\mu_l h_{fg}} = f(\frac{C_l \Delta T_{sub}}{h_{fg}}, \frac{\rho_l (u_m^2 \text{or} \bar{v}'^2) d_{32}}{\sigma}, \frac{a}{H}, \frac{\omega^2 a}{g}, \frac{\omega a}{u_d})$
			Flow rate	$\frac{qH}{\mu_l h_{fg}} = f(\frac{C_l \Delta T_{sub}}{h_{fg}}, \frac{\rho_l \sigma \dot{m}}{\mu_l^3} \text{or} \frac{\rho_l^2 \sigma v}{\mu_l^3}, \frac{\rho_l a \omega d_H}{\mu_l}, \frac{a}{H}, \frac{\omega^2 a}{g})$
	P_{ch}, ΔT_{sub}	4	Spray spec.	$\frac{qH}{\mu_l h_{fg}} = f(\frac{\rho_l (u_m^2 \text{or} \bar{v}'^2) d_{32}}{\sigma}, \frac{a}{H}, \frac{\omega^2 a}{g}, \frac{\omega a}{u_d})$
			Flow rate	$\frac{qH}{\mu_l h_{fg}} = f(\frac{\rho_l \sigma \dot{m}}{\mu_l^3} \text{or} \frac{\rho_l^2 \sigma v}{\mu_l^3}, \frac{\rho_l a \omega d_H}{\mu_l}, \frac{a}{H}, \frac{\omega^2 a}{g})$

[1]Chamber pressure is constant, [2]Chamber pressure and degrees of subcooling are constant, [3]Spray specifications

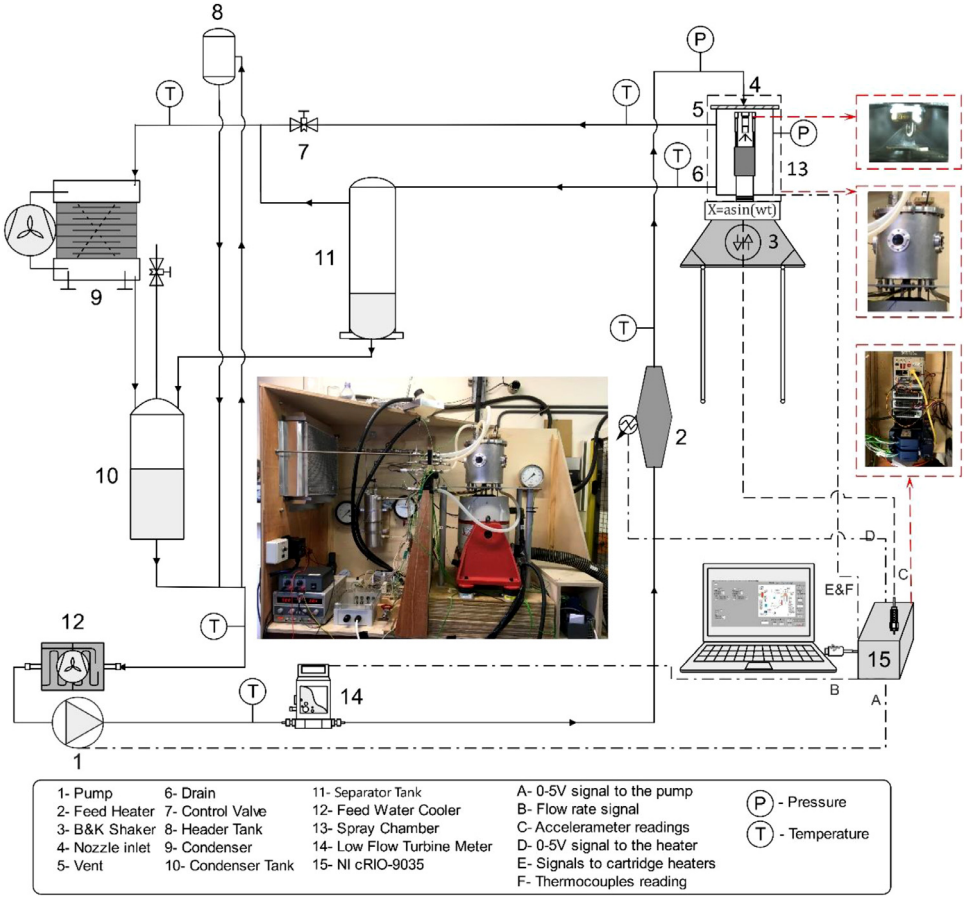

Fig. 1. Layout of the experimental hardware and the DAQ system.

3. Experimental facilities

Since getting an understanding of the dependence of CHF on key parameters, and calibration of the correlation modelling approach described in Section 2, requires measured experimental data, this section describes the facilities used. Fig. 1 shows both the experimental test rig used and the data acquisition system. The test rig comprised a spray chamber containing the test piece and a flow loop. The flow loop delivers de-ionised water at the desired operating conditions through stainless-steel piping to the spray nozzle inlet (No. 4). Three misting nozzles (of Type PJ8, PJ10, and MW145) are used (whose spray specifications are described in Section 3). During spray cooling, the accumulated water at the bottom of the spray chamber (No. 13) drained (No. 6) into the separator tank (No. 11), and the vapour in the chamber vented (No. 5) into an air-cooled condenser (Denso RDP 583, No. 9). Finally, the condensed water is cooled by a miniature heat exchanger (No. 12) to a temperature of less than 55 °C before entering the pump. There is also a header tank (No. 8) that removes any air from the system. This completes the flow loop.

The operating conditions are set using the gear pump (Micropumps MGD100P, No. 1) and pre-heaters (No. 2) through the DAQ system and its control unit. Both pump and band heaters are connected to the controllers in order to satisfy: flow rate, nozzle pres-

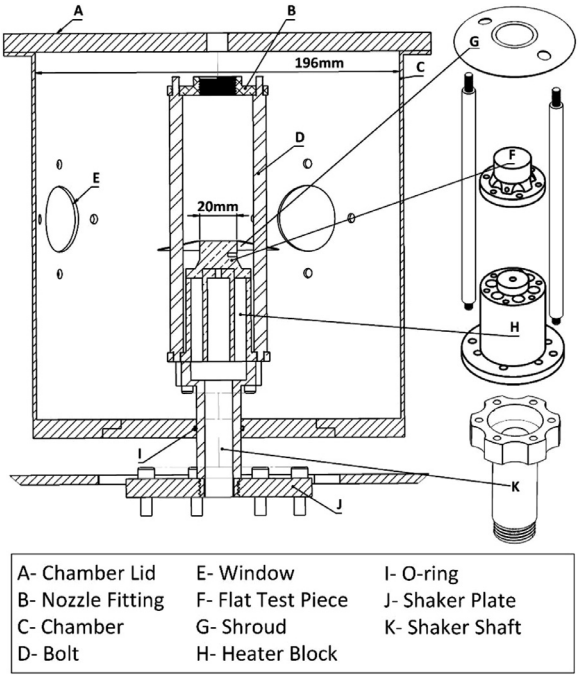

Fig. 2. Spray chamber cross-sectional view showing exploded view of copper test piece and heater block.

sure drop, and the inlet temperature control to set different subcooling degrees. The DAQ system comprises the main processor (NI cRIO-9035, No. 15) and C series modules which control the signals to the pump (A), 6×250 W cartridge heaters (E) and 2×345 W preheaters (D) using two (EVR-25BF) power regulators.

The NI Compact Rio system, in conjunction with the Human-Machine interface (LabVIEW on Windows desktop), monitors the signals from flow meter (B), accelerometer (C), and test piece thermocouples (F). The flow meter (No. 14) is a low-flow turbine meter (Omega FLR1009ST-D). There are two pressure transducers (Omega PXM309), i.e. one just before the nozzle inlet, and one connected to the chamber to capture the nozzle inlet (No. 4) pressure, the nozzle pressure-drop, and the spray chamber pressure (No. 13).

A more detailed view of the test-piece located in the spray chamber of Fig. 1, is shown in Fig. 2. Different spray nozzles are fitted on the top of the flat test-piece via nozzle fitting (B) and two long bolts (D). A shroud (G) is fitted around the test-piece to prevent spray impingement on the heater block to ensure one-dimensional heat transfer. The nozzle, two bolts, the shroud, the test piece, and the heater block, are shown located on top of a Bruel & Kjaer V555 mechanical shaker using a shaker shaft (K). The shaker (which drives the shaft through a joint in the shaker plate (J)) simulates vibration at appropriate amplitudes and frequencies chosen using a Feedback Instruments FG600 signal generator. A Piezotronics PCB A 353B15 accelerometer is also attached, to the bottom of the shaker plate.

Choosing an appropriate type of metal for the flat test-piece and heater-block is important in order to be able to accurately measure critical heat flux. Mudawar and Valentine [30] reported that using aluminium for the heater-block led to uncertainty in the repeatability of measurements owing to the high oxidation rate of aluminium (leading to their choice of copper based on the findings of Baumeister and Simon [64] who actually suggested similar results between copper and aluminium owing to their high thermal conductivity and near isothermal surface conditions. For this reason, high-purity copper was chosen for the test-piece and heater-block, with a thermal conductivity of 390 W/m^{2}K which has a near-constant value over the experimental test range.

4. Experimental test procedure and data reduction

The experimental test procedure to generate the required data to meet the objectives are shown in Table 4 along with the operating conditions. A chamber pressure of 1 bar, and a surface-to-nozzle distance of 12 mm, are kept constant. Three different nozzles are studied with their respective volumetric flow rates given in parenthesis namely for a type PJ8 (55 ml/min), a PJ10 (75-100 ml/min), and an MW145 (55 ml/min). For all tests, two subcooling temperatures are considered at 10 °C and 45 °C. Testing involving a total of 64 cases included the cooling surface having no vibration, referred to as 'static', plus dynamic cases with different vibration amplitudes and frequencies labelled in the last column of Table 4. The spray specifications associated with the operating conditions are also shown in Table 4.

At the beginning of each test (with or without vibration), the power was supplied to the cartridge heaters to bring the cooling surface to a condition within the two-phase heat transfer mode. Steady-state was assumed to occur when all temperature differences associated with all three thermocouples (in time intervals of three minutes) were less than 0.3 °C (as convergence criterion). The power was then gradually increased until the CHF occurred. The heat flux was calculated from the readings of the uniform temperature gradient between three thermocouples evenly spaced 5.5 millimetre apart. During the experiments, linearity of temperature measurements was monitored to ensure one-dimensional heat transfer. This measure justifies a predictive solution using the one-dimensional conduction equation:

$$q = -K\frac{dT}{dx} \tag{5}$$

where K, dT, and dx are the thermal conductivity, the temperature difference, and the distance between the top and bottom thermocouples located in the test-piece. The surface temperature was obtained by extrapolating the linear temperature distribution to the surface (as done by Mudawar and Valentine in [30]).

Uncertainty analysis using Moffat's method [65] was undertaken. Results show that the maximum uncertainty in the calculation of heat flux at the maximum measured data point of 2.67 MW/m^2 is predicted to be 2.57%. Table 5 shows the measurement errors and calculated parameter uncertainties.

Considerable care has been taken to identify the key factors involved in successful reproducibility of the data. A regular change of de-ionized water, and checking that the cooled disc has the same surface roughness using the same abrasive paper (and therefore ensuring no copper oxidation), was found to be the most important precautions required to be able to undertake experiments on different days.

For the sake of maximum reliability in the reproducibility of the data, each case in Fig. 3 has been repeated twice on two different days - only cases with the largest deviation are reported. At the start of each day, the de-ionized water was replaced, and the copper surface was polished with a wet-dry paper. As can be seen, the maximum deviations for CHF are less than predicted by uncertainty analysis, except for MW145 (4%). For the excess temperature, the average deviation is higher than the thermocouples uncertainty. For that reason, the maximum deviations caused to CHF (for MW145), and the excess-temperature-during-repeatability analysis, has been taken into consideration to interpret the data, and the trends in the results. It should be noted however, that test runs for each nozzle, were actually taken on the same day to minimise the effect of reproducibility and to maximise the reliability in the comparisons.

Table 4
Test plan and spray specification for the operating conditions of the PJ and MW145 nozzles.

$P_{chamber}$ (bar)	v (ml/min)	ΔT_{sub} (°C)	H (mm)	Static	f (Hz) / a (mm)	2	4	8	50	50	100	200	Case
1	55, 75 and 100	10 and 45	12	✓	8	✓	-	-	-	-	-	-	D-1
					4	-	✓	-	-	-	-	-	D-2
					1	-	-	✓		-	-	-	D-3
					1	-	-	-	✓		-	-	D-4
					0.2	-	-	-	-	✓	-	-	D-5
					0.2	-	-	-	-	-	✓	-	D-6
					0.04	-	-	-	-	-	-	✓	D-7

NOZZLE SPRAY SPECIFICATIONS

Nozzle	d_n (mm)	α (°)	Covering d. (mm)	ΔP (bar)	$u_m(\frac{m}{s})$	d_{05} (μm)	d_{32} (μm)
PJ8	0.20	90	24	4.7	31.3	22	107
PJ10	0.25	90	24	2.9-5.2	24.6-32.9	26-33	117-137
MW145	0.41	70	17	7	38.2	47	141

Table 5
Uncertainties in the calculated and measured parameters.

Parameter	Uncertainty (%)	Units
Thermocouples	±0.4	°C
Volumetric flow rate	±0.6 (of full scale)	ml/min
Accelerometer frequency	±5	Hz
Length	±1	mm
Heat flux	±2.57	MW/m^2

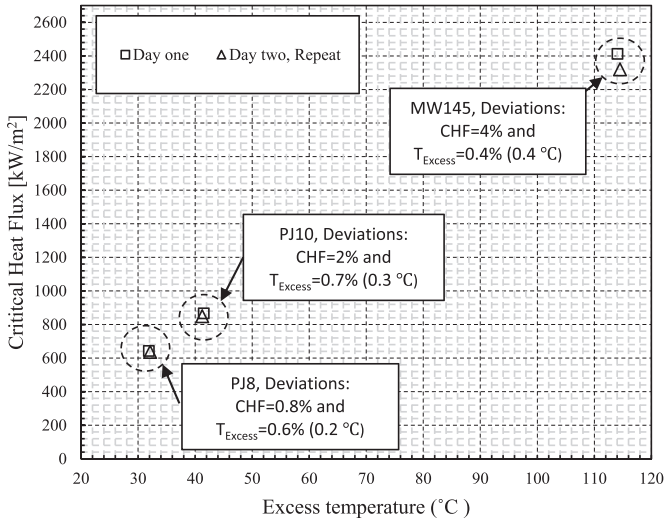

Fig. 3. CHF and excess temperature maximum deviations to reproducibility of the results.

5. Results and Discussion

In this section, the influence of surface vibration on the CHF and excess temperature are discussed. First, the effect of flow rate and degrees of subcooling with, and without vibration has been examined. This is to help understand the physics behind the trends in the data, which are useful for modelling. Second, the effect of vibration on the excess temperature at CHF has been investigated in detail. The maximum achievable temperature is a key parameter due to its importance for thermal management applications, especially in the safety mode. Finally, correlation models discussed in Section 2, have been calibrated for prediction of CHF and maximum temperature.

5.1. Effect of nozzle flow parameters and degrees of subcooling for static surfaces

Flow rate and pressure drop are nozzle flow parameters. Fig. 4a shows the CHF variation with three volumetric flow rates of 55 ml/min, 75 ml/min and 100 ml/min for PJ8, PJ10, and MW145 nozzles. As can be seen for the PJ8 and PJ10 nozzles, CHF increases with flow rate, and this trend is valid for both degrees of subcooling (i.e. 10 and 45 °C). Toda and Uchida [66], Hou et al. [67], Chow et al. [68], Moreno et al. [69], Estes and Mudawar [49] and Pais et al. [70] all reported that increasing flow rate increases CHF. However, CHF for MW145 has an almost three-fold increase in comparison with those for PJ nozzles, even though the flow rate for MW145 is 55 ml/min, suggesting that the CHF does not always increase with volumetric flow rate. Chen et al. [71] and Tilton [72] suggested that the volumetric flow rate has only a subtle, or even no influence, on CHF. The higher CHF for the MW145 is a result of a higher nozzle pressure drop (i.e. 7 bar, in contrast to 2.9 to 5.2 bar for PJ nozzles), but also from different geometrical parameters (e.g. nozzle orifice and cone angle, see Table 4) which changes hydrodynamic parameters (such as mean droplet velocity).

Fig. 4b shows the same CHF results plotted as a function of average volumetric spray flux for each nozzle. Chen et al. [71], Estes and Mudawar [49], Pais et al. [70], Lin and Ponnappan [73], and Monde [74] have all suggested that CHF for different nozzles, increases with volumetric flux with no reverse trends. Fig. 4b shows the same behaviour for different nozzles namely: PJ8 (0.77×10^{-3}m^{3}s^{-1}/m^2), PJ10 (1.05×10^{-3}-1.40×10^{-3} m^{3}s^{-1}/m^2), and MW145 (9.03×10^{-3}m^{3}s^{-1}/m^2).

The average volumetric flux, $\bar{v}''$, is proportional to volumetric flow rate, v, and can be calculated according to Eq. (2) [75]:

$$\bar{v}^{\prime\prime}{}_{prime} = \frac{v}{\pi\left(H tan\left(\frac{\alpha}{2}\right)\right)^2} \tag{6}$$

where H is nozzle-to-surface distance and α is the spray cone angle. Fig. 4a also shows the subcooling impact on CHF. For the PJ8 and MW145 nozzles with a lower flow rate of 55 ml/min, CHF decreases by the higher subcooled conditions of 45 °C. As can be seen, the deviations for the PJ8 and MW145 are respectively 18% and 11%. This means that the CHF acquires a higher value as soon

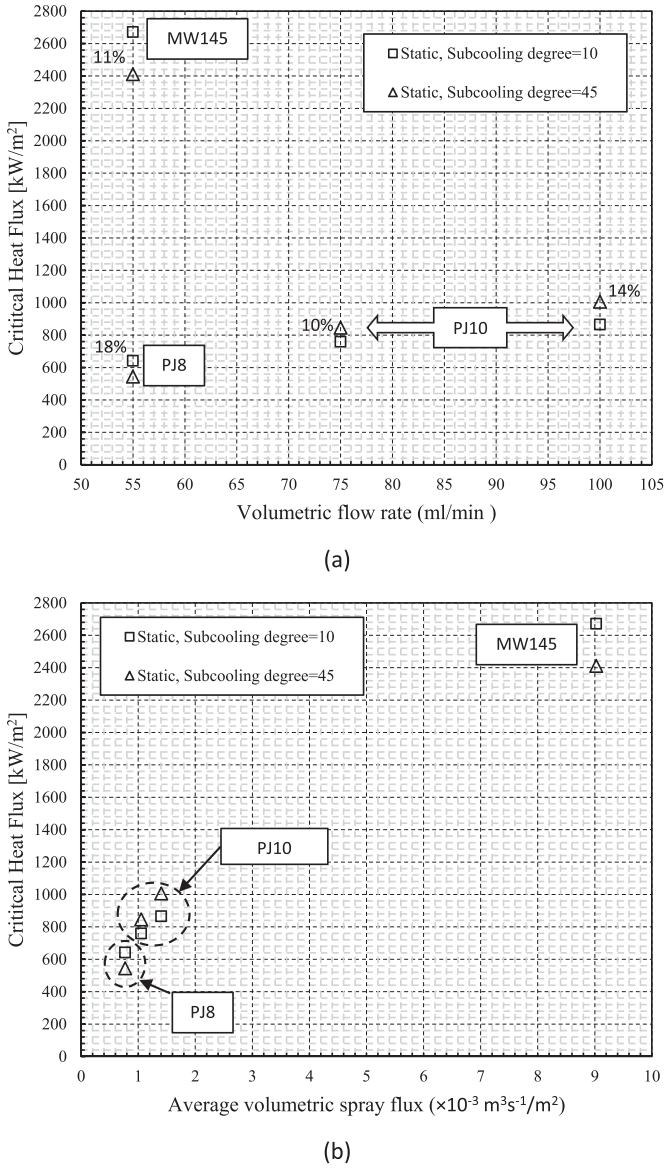

Fig. 4. CHF trend for static cooling surfaces based on nozzle flow parameters and degrees of subcooling.

as subcooling is closer to saturated conditions. Thiagarajan et al. [52] reported the same behaviour for the subcooling influence of low flow rate sprays. Conversely, for the PJ10 with higher flow rates of 75 and 100 ml/min, a higher subcooling degree of 45 °C enhances the CHF by 10% and 14% respectively. Visaria and Mudawar [76] found a similar trend in their data with subcooling degrees between 22 °C and 70 °C. In the experiments in [76], it was noted that the CHF enhancement is more substantial when the subcooling degree exceeds 40 °C. Overall, the trends in the CHF data for static surfaces are in good agreement with the literature. In the next section, the effects of the vibrating surfaces on the CHF as well as excess temperature will be discussed.

5.2. The effect of vibrating surfaces on CHF and excess temperature

In this section the effects of vibration on CHF and excess temperature for all three nozzles of PJ8, PJ10 and MW145 is assessed. The CHF data for static and dynamic cases are examined as a function of excess temperature, subcooling degrees, and volumetric flux to better understand the combined effect of different parameters. An 'effect ratio' is introduced, defined as the ratio of the dynamic-CHF/static-CHF which is shown versus excess temperature. For subplots containing two subcooling degrees and flow rates in which there are two comparable static cases, the effect ratio also includes corresponding static-CHF/static-CHF. Therefore, to make different effect ratios identifiable, three effect ratios are defined and used in corresponding subplots. First, a dynamic effect ratio θ_{Dyn} is defined as the ratio of the dynamic-CHF/static-CHF. Second, a volumetric flux effect ratio θ_{ν}'' includes both dynamic-CHF/static-CHF and corresponding static-CHF/static-CHF ratios. Third, a subcooling effect ratio θ_{SC} , includes both dynamic-CHF/static-CHF and corresponding static-CHF/static-CHF ratios. To make room for inspection it is useful to define considered vibrational ranges. Large-amplitude vibrations include data points with amplitudes from 1 to 8 mm and frequencies up to 8Hz (the first three dynamic cases). High-frequency vibrations are the dynamic cases with a frequency above 50Hz and amplitudes smaller than 1mm (the last three dynamic cases). The dynamic case with a=1mm and f=50Hz corresponds to the highest Vibrational Reynolds Number of 21360, and the largest Acceleration Number of 10. These numbers are supplied in Table 6 (each row is related to the same case in the legends of the figures).

Vibrational Reynolds number and dimensionless Acceleration number are helpful in assessing the combined influence of surface amplitude and frequency at CHF. Figs. 5 and 6 demonstrate all the data points (CHF versus volumetric flux) for PJ8, PJ10 and MW145 nozzles respectively at two subcooling degrees of 10 and 45 °C.

At first, the general trend in Figs. 5a and 6a shows that CHF increases for dynamic cases with increasing volumetric flux. Considering the effect ratios on Figs. 5 and 6, the enhancement for SC=45°C is more appreciable. However, there are two exceptions in Figs. 5b and 6b, including the results for PJ nozzles. These exceptions relate to the dynamic case D-7 with the highest frequency. One is at SC=10 °C for PJ8 (Fig. 5b), for which the D-7 case (at $\bar{\nu}''= 0.77 \times 10^{-3}m^3s^{-1}/m^2$) has a greater CHF value compared to those for D-6, D-5 and D-4 cases of PJ10 with a greater volumetric flux of $1.05 \times 10^{-3}m^3s^{-1}/m^2$. The effect ratio of PJ8-D-7 is 1% greater than PJ10-D-6, and 2% greater than PJ10-D-5 and PJ10-D-4 cases.

The second occurs at SC=45 °C for case D-7 of the PJ10 (Fig. 6.b) at $\bar{\nu}'' = 1.05 \times 10^{-3}m^3s^{-1}/m^2$, at which the CHF acquires a slightly greater value than D-4 at $\bar{\nu}''= 1.40 \times 10^{-3}m^3s^{-1}/m^2$ (where the effect ratios for D-7 and D-4 at these volumetric fluxes are 1.60 and 1.59 respectively). As mentioned, D-4 has a larger amplitude and a lower frequency and the highest Reynolds Number. The reason for this reverse trend can be attributed to the enhancing effect of vibration for the D-7 cases of PJ nozzles. However, further investigation is required to precisely explain the effects of different elements of vibration such as amplitude and frequency, as well as the effect of Acceleration and Reynolds Number. In the next subsections the influences of different key parameters are discussed.

Figs. 5b and 6b show the results of the PJ8 and PJ10 nozzles (as expanded versions). This is to investigate the effect of volumetric flux and compare it with what was found for the static cases in the previous section.

5.2.1. The largest deviation from the static CHF and the effects of Subcooling degrees

Figs. 7 and 8 show the results for the PJ10 nozzle at coolant flow rates of 75 ml/min and 100 ml/min respectively. Figs. 9 and 10 show corresponding results for the PJ8 and MW145 nozzles. As can be seen from Figs. 7 to 10, the CHF for the dynamic cases involving large-amplitude or high-frequency vibration result in a deviation from the corresponding static results. For the PJ10, as seen in Figs. 7 and 8 (for both subcooling degrees in respective subplots a and b) the largest deviation from the static CHF belongs to the case

Table 6
Static and dynamic cases with associated Acceleration and Vibrational Reynolds numbers.

Test case	Amplitude (mm)	Frequency (Hz)	Vibrational Reynolds Number (-)	Acceleration Number (unit of g)
S	0	0	0	0
D-1	8	2	6835.2	0.13
D-2	4	4	6835.2	0.26
D-3	1	8	3417.6	0.26
D-4	1	50	21360	10.06
D-5	0.2	50	4272	2.01
D-6	0.2	100	8544	8.05
D-7	0.04	200	3417.6	6.44

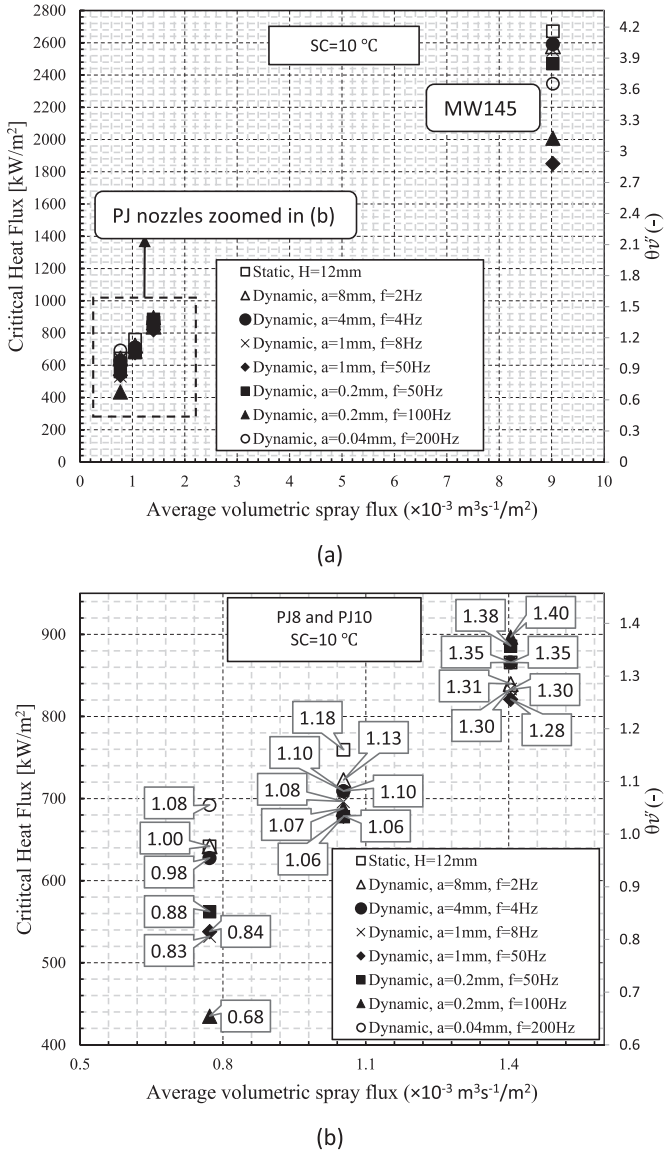

Fig. 5. Measured CHF versus volumetric flux at SC=10 °C : a) PJ and MW145 database b) zoomed version of PJ8 and PJ10 test cases.

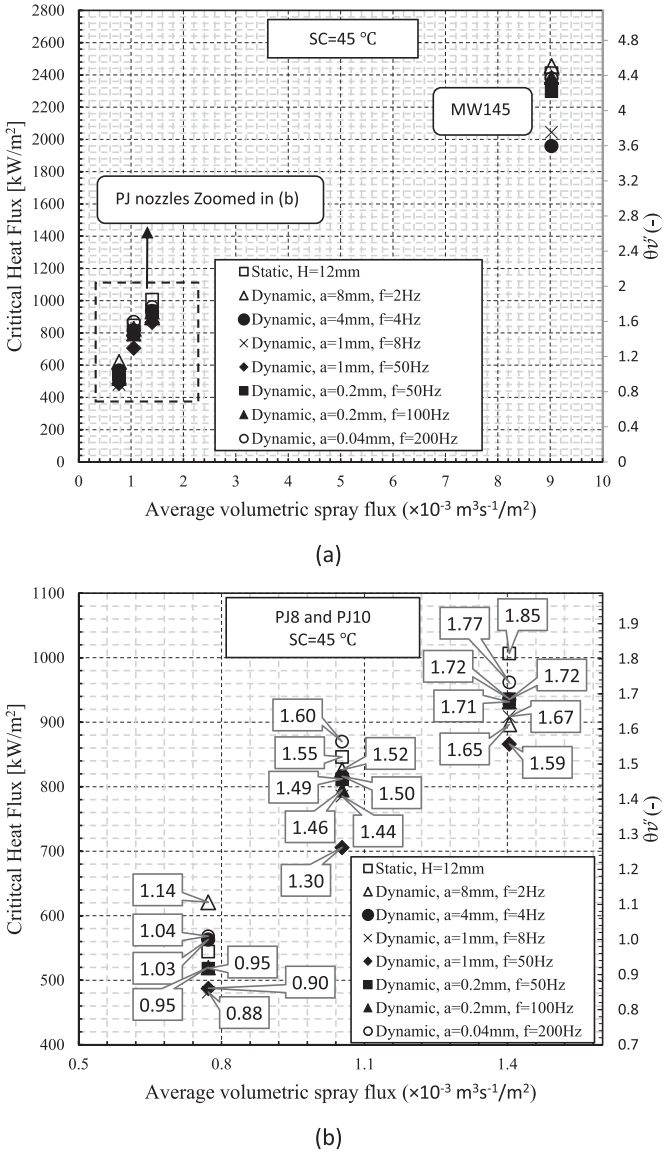

Fig. 6. Measured CHF versus volumetric flux at SC=45 °C: a) PJ and MW145 database b) zoomed version of PJ8 and PJ10 test cases.

D-4 with a=1 mm and f=50 Hz, and with the highest Reynolds Number and largest Acceleration Number (See the effect ratios in Figs. 7 and 8, and for cases D-2, D-3, D-4, and D-7, in Table 7). For the flow rate of 75ml/min, at subcooling of 10 °C (Fig. 7a) the effect ratio for case D-4 is 89 percent. And at subcooling of 45 °C (Fig. 7b) the effect ratio is 83 per cent. It is evident that the deteriorating effect of vibration for the dynamic case D-4 (as shown by a diamond marker) becomes more appreciable by increasing the subcooling degree. The same behaviour for the same test case of D-4 can be seen in Fig. 8 for the flow rate of 100 ml/min. Figs. 8a and 8b, at the subcooling of 10 °C, show that the smallest effect ratio is 95 per cent which reduces to 86 per cent at the subcooling of 45 °C.

For the PJ8 nozzle, D-6 has the lowest effect ratio of 68% at SC=10 °C (Fig. 9a). However, by increasing the subcooling to 45 °C, the impeding effect of vibration reduces and the D-6 datapoint has

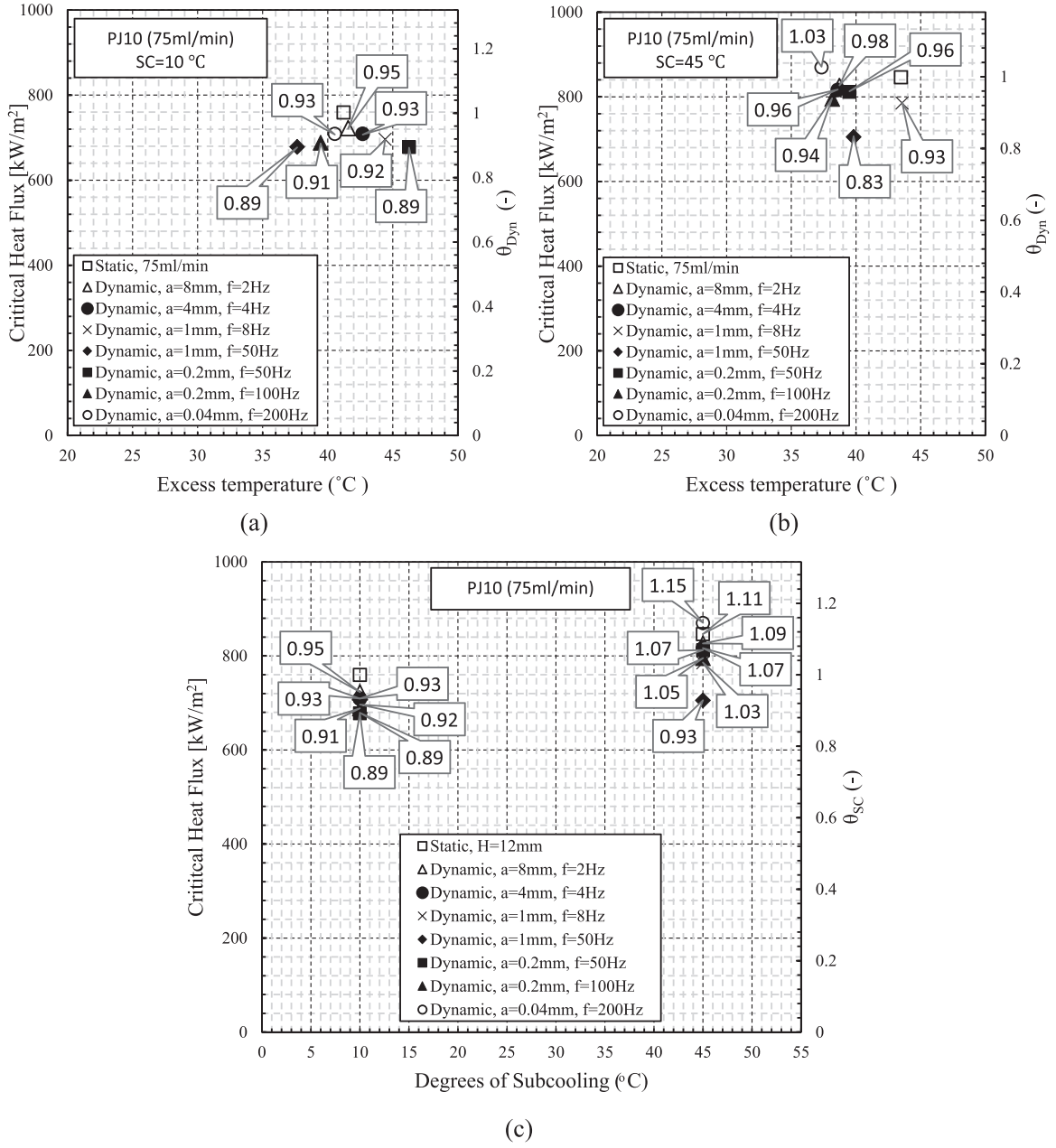

Fig. 7. Measured CHF for the PJ10 nozzle at 75 ml/min versus excess temperature at $SC = 10^{\circ}C$ (a) and $SC = 45^{\circ}C$ (b), and the effect of subcooling on CHF (c) for the case studies involving static and dynamic cooling surfaces.

a 95% deviation. The same behaviour is evident for the MW145. The lowest effect ratio of 69% (for D-4 at 10 °C subcooling) increased up to 98% at 45 °C of subcooling (Fig. 10). This is the exact opposite to that found for the PJ10 with the response of its lowest effect ratio to subcooling. The reason for this can be associated with the reverse heat transfer trend (as was found in the previous section for static cases) stemming from the subcooling effect at low flow rate for the PJ8 and MW145 nozzles in comparison to the higher flow rate of the PJ10 nozzle.

To investigate this reverse trend, the influence of subcooling on the dynamic-CHF data and a comparison of the behaviour with the static cases in the previous section is examined, particularly Subplots c in Figs. 7 to 10. For the PJ10 nozzle (at both flow rates in Figs. 7c and 8c), the effect ratio for every dynamic case has been increased by augmenting the subcooling degree. It is still following the same trend (as in the previous section). Therefore, increasing subcooling degrees for the PJ10 increases CHF for its static and dynamic cases. By contrast, for the PJ8 and MW145, the behaviour should be the exact opposite of the PJ10 trend (as was found for the static cases). But inspecting the effect ratios in Figs. 9c and 10c suggests this trend is still valid apart from two high-frequency vibration cases: D-6 (for the PJ8 and MW145) and D-4 (for the MW145 only). The CHF for case D-6 at SC=45 °C have higher values for both the PJ-8 and MW145. The CHF for D-4 case of the MW145 nozzle reaches a higher value at the higher subcooling of 45 °C. This clearly shows that surface vibration causes a change in the trend identified. To reveal this further, the effect of vibration, in particular the influence of amplitude and frequency, is now examined in more detail.

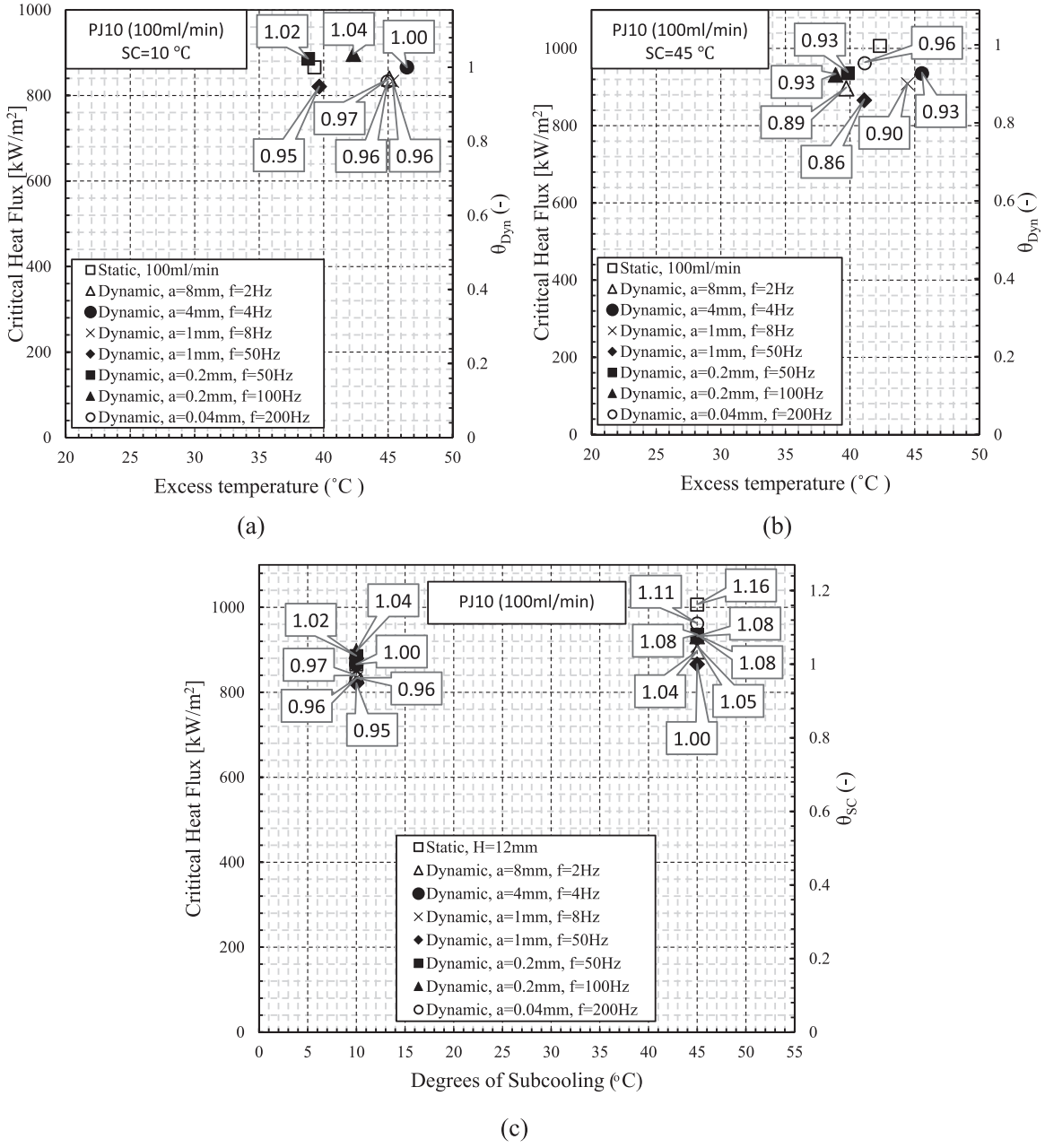

Fig. 8. Measured CHF for the PJ10 nozzle at 100 ml/min versus excess temperature at $SC = 10^{\circ}C$ (a) and $SC = 45^{\circ}C$ (b), and the effect of subcooling on CHF (c) for the case studies involving static and dynamic cooling surfaces.

5.2.2. The effect of vibrating surface amplitude and frequency on CHF

To establish whether the amplitude of a vibrating surface has any impact on the dynamic-CHF, the cases D-5 (a=0.2mm) and D-4 (a=1mm) at a frequency of 50Hz are examined. The D-5 and D-4 cases are respectively shown in Figs. 7 to 10 with square and diamond markers. For the PJ10 nozzle, the amplitude has a deteriorating effect on CHF (except for flow rate 75 ml/min and subcooling of 10 °C, that amplitude has no effect). The highest impeding effect of 13 percent occurs for the flow rate of 75 ml/min at subcooling of 45 °C (on Fig. 7b, D-5 and D-4 effect ratios are 0.96 and 0.83). At the flow rate of 100 ml/min (Fig. 8), this deterioration effect, for both subcooling degrees, is 7 percent. The results for the PJ8 (Fig. 9) support the argument suggesting the impeding effect of amplitude on CHF. For subcooling degrees of 10 and 45 °C, the impeding effects are respectively 4 and 5 percent. Therefore, the subcooling influence is only 1 per cent. However, for MW145, at subcooling of 45 °C (Fig. 10b), vibration amplitude shows an enhancing influence. To address this reverse trend, the frequency element of vibration is now examined.

To assess the effect of frequency of a vibrating surface, cases D-3 (f=8Hz) and D-4 (f=50Hz), with an amplitude of a=1mm are examined. The data associated with D-3 and D-4 cases are respectively shown by cross and diamond markers. For these two cases for the MW145 at SC=45 °C (Fig. 10b), the frequency causes a 13% enhancement (For D-3 the effect ratio is 0.85, and for D-4 it is 0.98). But for SC=10 °C (Fig. 10a), vibration frequency causes a 27% deterioration. Comparing the effects of amplitude and frequency for the MW145 suggests that vibration frequency plays a dominant role. Small heat transfer enhancements are also evident in Figs. 9a (1% increase at SC=10 °C) and 9b (2% enhancement at SC=45 °C) for the PJ8. For the PJ10 (Figs. 7 and 8), for all the flow rates and levels of subcooling, vibration frequency has a deterio-

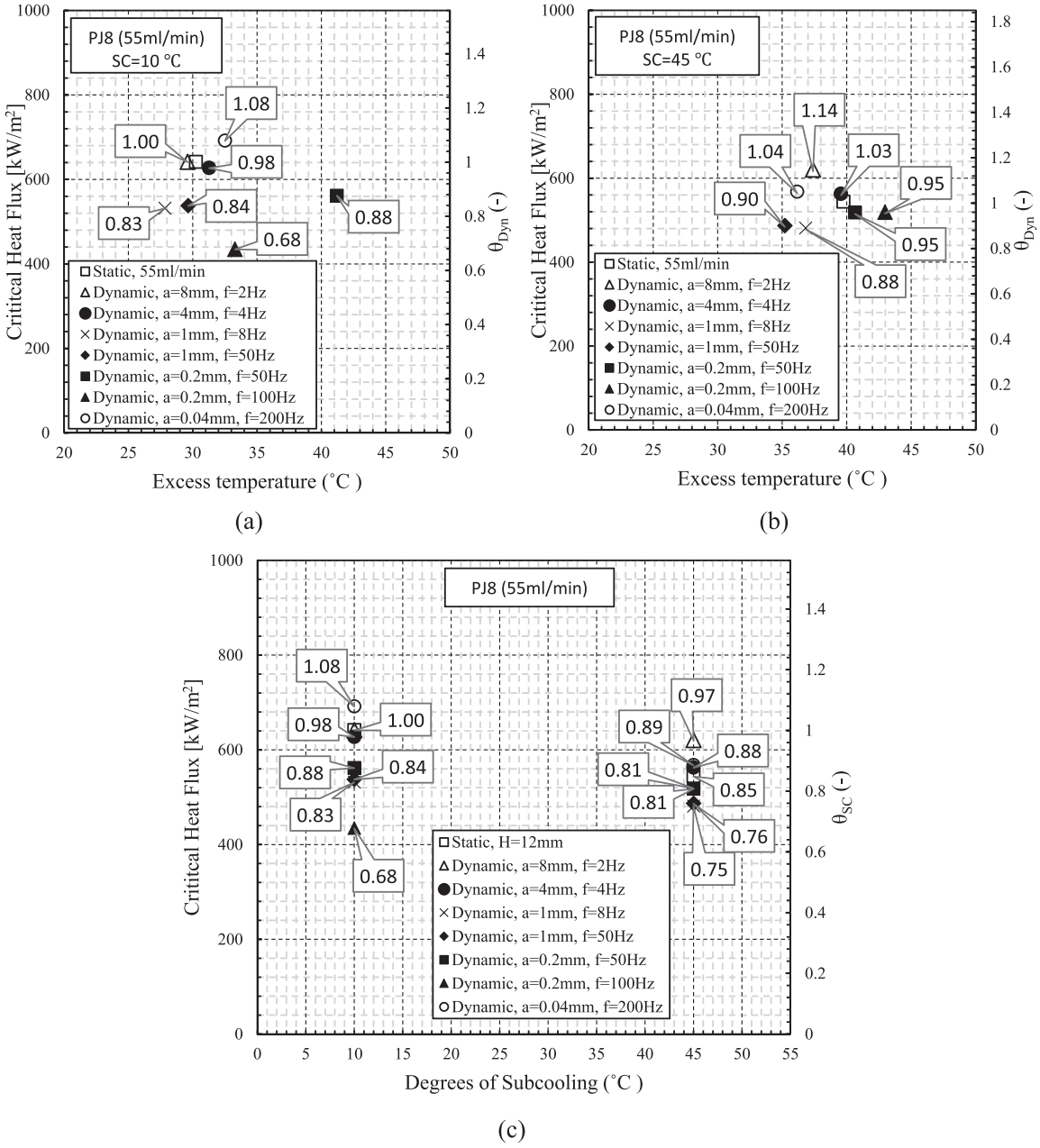

Fig. 9. Measured CHF for the PJ8 nozzle versus excess temperature at $SC = 10°C$ (a) and $SC = 45°C$ (b), and the effect of subcooling on CHF (c) for the case studies involving static and dynamic cooling surfaces.

rating effect on the dynamic-CHF. The differences between these two cases in Figs. 7a (SC=10 °C), 7b (SC=45 °C), 8a (SC=10 °C), and 8b (SC=45 °C) are respectively 3%, 10%, 1% and 4%. The impeding effect is more considerable for higher subcooling degrees of 45 °C. It is evident that by increasing the flow rate, the deteriorating influence decreases. Vibration frequency and amplitude are probably better understood in terms of non-dimensional vibration parameters whose examination should better explain such contradictory behaviour. The next section, examines the effect of vibration specifically in terms of Vibrational Reynolds Number and Acceleration Number.

5.2.3. The influence on CHF of Vibrational Reynolds Number and Acceleration Number

The influence on CHF of Vibrational Reynolds Number and Acceleration Number are now explained. Interpretation of the data has been achieved by reviewing dynamic effect ratios for the chosen dynamic cases in Table 7 in conjunction with observation in Fig. 11 of CHF data trends when viewed as functions of both non-dimensional numbers. Vibrational Reynolds Number and Acceleration Number are useful for representing the dynamic nature of the spray field on a vibrating surface, such as the effect on droplet rebound, splash and liquid film thinning. These dimensional parameters are used to investigate the complex effects of vibration on the heat transfer mechanisms. To assess the influence of Vibrational Reynolds Number, cases D-3 (Re=3417.6) and D-2 (Re=6835.2) with the same Acceleration Number of 0.26 are considered. Comparison of all data points of D-3 and D-2 in Figs. 7 and 8, reveal that for both flow rates and subcooling degrees of the PJ10 nozzle, increasing Reynolds Number from 3417.6 to 6835.2, first enhances the CHF, but then impedes it for the highest Reynolds Number (Re=21360, D-4). To support this claim, all the associated effect ra-

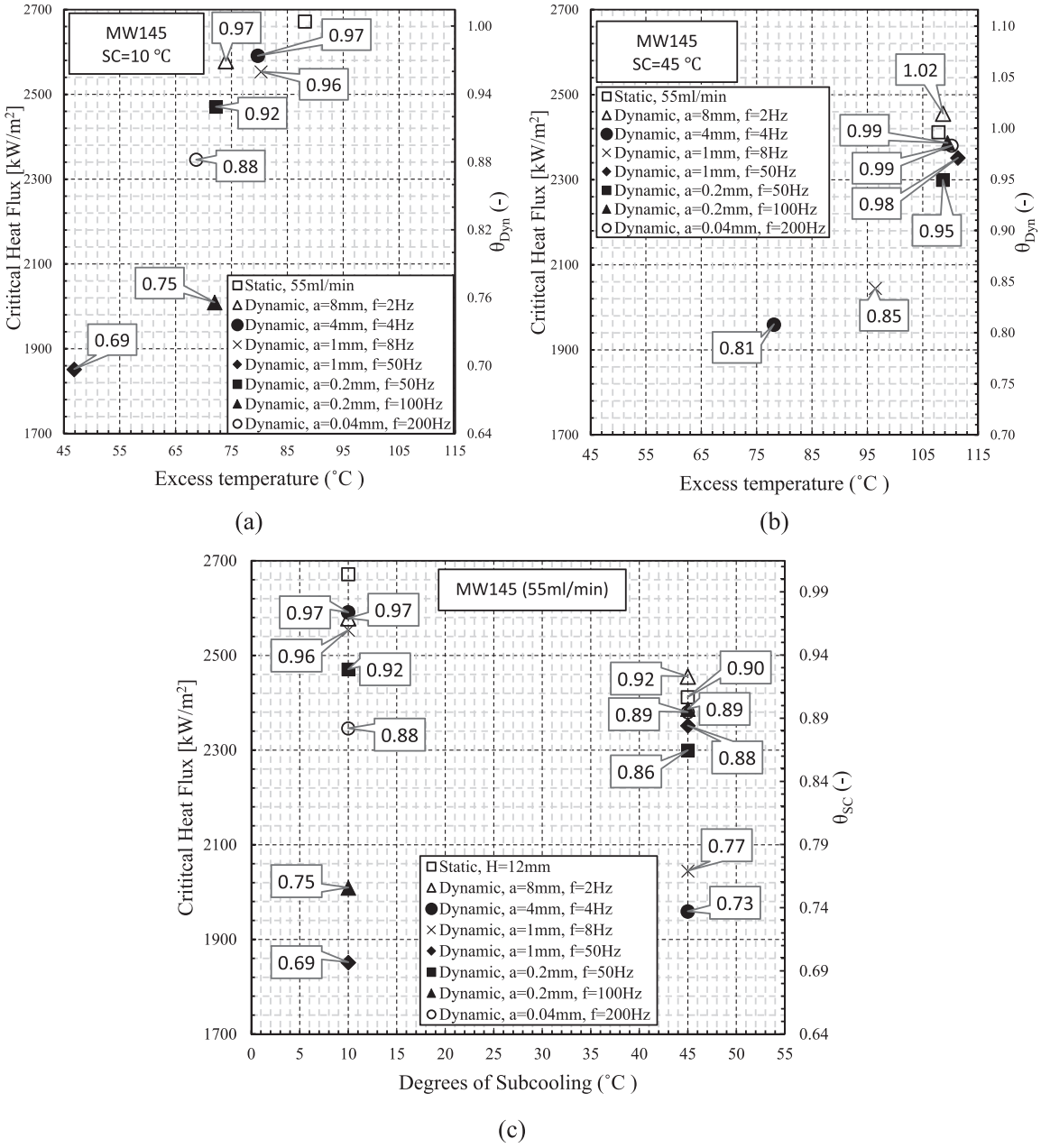

Fig. 10. Measured CHF for the MW145 nozzle versus excess temperature at $SC = 10°C$ (a) and $SC = 45°C$ (b), and the effect of subcooling on CHF (c) for the case studies involving static and dynamic cooling surfaces.

tios are supplied in Table 7 for ease of reading. For all data points in Table 7, the associated CHF values against Reynolds and Acceleration numbers are plotted in Fig. 11 to facilitate the interpretation of the trends. For flow rate 75ml/min, at SC=10 °C (Fig. 7a), the effect ratio of D-3, D-2 and D-4 are respectively: 0.92, 0.93, 0.89. For the same flow rate, at SC=45 °C (Fig. 7b), the effect ratios of D-3, D-2 and D-4 are 0.93, 0.96, 0.83. As can be seen from Table 7, PJ nozzles follow the behaviour mentioned for all the flow rates and subcooling degrees (as can also be seen in Fig. 11a). The only exception is the MW145 at SC=45 °C for which the effect ratio is first reduced through an increase in Reynolds Number (3417.6 to 6835.2), and then increased for the highest Reynolds Number. This is different from the trend of the other cases. For the MW145 nozzle, the opposite behaviour can be explained by its high dependency on the subcooling effect. The spray field for MW145 is a light fog resulting in a thinner liquid film on top of the cooling disc, whereas for the (misting) PJ nozzles it has a relatively thicker liquid film (observed) during the experiments. For this reason, it appears that the MW145 nozzle is less dependent on Reynolds Number and Acceleration Number.

To explore the effect of acceleration, the results for test cases of D-3 (Ac=0.26) and D-7 (Ac=6.44), both cases with a Reynolds Number of 3417.6, are compared in Table 7 (as also shown in Fig. 11b). For PJ nozzles, CHF associated to D-7 are all enhanced by the larger Acceleration Number except for a flow rate 100ml/min at subcooling of 10 °C which Acceleration Number does not have any influence on CHF. The enhancing effect of acceleration conform to the results of Michalak et al. [44] for the acceleration range of $0.15g < Ac < 1.80g$. However, there are other studies such as work of Zhang et al. [77,78], and Conrad et al. [79], suggesting that the acceleration enhancement is limited to the operating conditions, and other parameters are the main determinant of the heat flux.

Table 7
Dynamic effect ratios for the chosen dynamic cases to explore the Vibrational Reynolds and Acceleration effects.

	PJ10				PJ8		MW145			
Flow rate (ml/min)	75		100		55		55		Re_V	Ac
Subcooling (°C)	10	45	10	45	10	45	10	45		
D-3	0.92	0.93	0.96	0.90	0.83	0.88	0.96	0.85	3417.6	0.26
D-2	0.93	0.96	1	0.93	0.98	1.03	0.97	0.81	6835.2	0.26
D-4	0.89	0.83	0.95	0.86	0.83	0.90	0.69	0.98	21360	10.06
D-7	0.93	1.03	0.96	0.96	1.08	1.04	0.88	0.99	3417.6	6.44

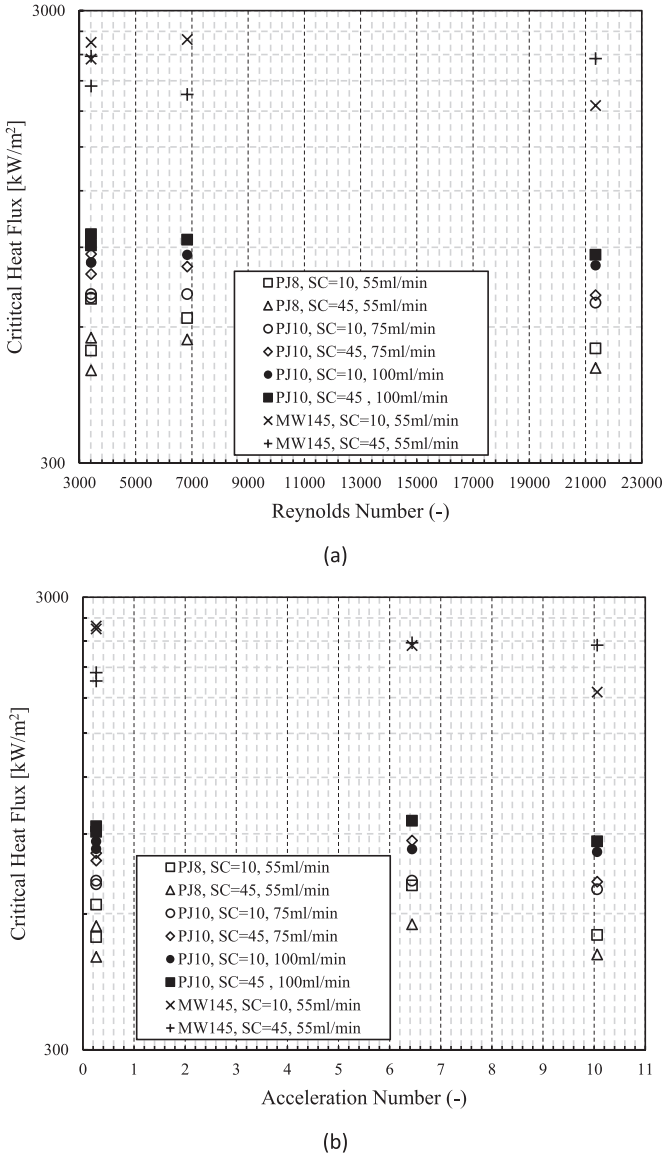

Fig. 11. Vibrational Reynolds Number effect (a), and Acceleration Number effect (b), for the chosen dynamic cases in Table 7.

For the MW145, at SC=10 °C there is a reduction in the effect ratio for D-3 and D-7 which shows that other key parameters determine this impeding effect. As was shown for the MW145 at SC=10 °C (in the previous section), the frequency has a noticeable deteriorating effect. Switching the frequency from 8Hz (D-3) to 200Hz for case D-7 supports the independence to Acceleration of the MW145 results. Another key parameter responsible for this reverse behaviour for Reynolds Number, can be the considerable effects of subcooling. In the next section, the complex effects of vibration and subcooling on the maximum temperature (at which CHF can occur) are investigated.

5.2.4. The effect of vibration on excess temperature

Further inspection of the subplots of Figs. 7a, 7b 8a, 8b, 9a, 9b, but also Fig. 10, it is noticeable that vibration changes the excess temperature at which the Static-CHF occurs. To explain the reason for this, as mentioned, Acceleration Number and Reynolds Number affect the dynamic behaviour of the spray field and consequently the heat transfer mechanisms. For instance, the vibration surfaces with different amplitude and frequencies can be responsible for thinning and thickening of the liquid film. These effects can either advance or delay the transition from nucleate boiling to transition boiling (where the maximum temperature and CHF occurs). In other words, thinning and thickening of the liquid film (which is two-phase in nature) can influence the chance of slug propagation and therefore promoting or delaying the incidence of the CHF. In addition, the fluctuating relative speeds due to the vibrating surfaces, changes the intensity of drop rebounding and splashing in the flow field. All the above mentioned are important in different heat transfer mechanisms involved in spray cooling. Table 8 shows the temperature differences between the dynamic and corresponding static cases for each nozzle and associated operating conditions.

The largest difference in the excess temperature of the dynamic cases from the static cases for PJ8 and PJ10 are for those with high-frequency vibrations with the exception of the PJ10 at 100 ml/min and SC=10 °C. For the MW145, the largest difference in the excess temperature occurred for the cases in high-frequency vibrations at SC=10 °C, while at SC= 45°C, the largest deviations are in the large-amplitude vibration range. For the PJ10 at 75 ml/min and SC=10 °C (Fig. 7a), this difference is -3.6 °C for case D-4, and 5°C for case D-5. At the subcooling of 45 °C (Fig. 7b), the excess temperature difference for case D-6 and D-7 are respectively -5.3°C and -6.1 °C. Test cases of D-4, D-5, D-6 and D-7 all have accelerations above 2g (see Table 6). Considering these test cases, for both subcooling degrees, as soon as the Acceleration and Vibrational Reynolds numbers decreased (from D-4 to D-5 and D-6 to D-7) the temperature difference has increased. At 100 ml/min and subcooling of 45 °C (Fig. 4b) the largest temperature difference also occurred for the case D-6 (3.4 °C) which is within the range of high-frequency vibrations. By contrast, at 100ml/min and subcooling of 10 °C (Fig. 4a), the large-amplitude vibrations on average caused the largest temperature deviation from that for the static case. The test case of D-2 has a temperature difference of 7.2 °C, and test cases of D-1 and D-3 have temperature differences of 5.8 °C and 6.0 °C. Table 6, giving the Acceleration Number and the Vibrational Reynolds Number for these cases, confirms that it is still valid to claim that decreasing these two dimensionless numbers the temperature difference increases. Case D-1 in comparison to D-2 has a smaller Acceleration Number but a fixed Re=6835, and Case D-3 has a lower Reynolds Number in comparison to Case D-2

Table 8
Temperature difference (°C) from static cases to inspect any effects of vibration on excess temperature.

	PJ10				PJ8		MW145	
Flow rate (ml/min)	75		100		55		55	
$\bar{v}''$ ($\times 10^{-3}$m^{3}s^{-1}/m^2)	1.05		1.40		0.77		9.03	
Subcooling (°C)	10	45	10	45	10	45	10	45
D-1	0.3	-4.8	5.8	-2.6	-0.6	-2.4	-14.2	0.8
D-2	1.5	-4.9	7.2	3.3	1.0	-0.2	-8.4	-29.7
D-3	3.2	0	6.0	2.1	-2.4	-2.9	-7.8	-11.4
D-4	-3.6	-3.7	0.4	-1.2	-0.6	-4.5	-41.3	3.5
D-5	5	-4	-0.5	-2.5	11	0.9	-15.9	0.8
D-6	-1.8	-5.3	3	-3.4	3	3.2	-16.2	1.6
D-7	-0.7	-6.1	5.7	-1.2	2.3	-3.6	-19.5	2.4

(while Ac=0.26). This shows the effect of vibration on effective excess temperature. The effect of Acceleration Number and Reynolds Number, in addition to frequency and amplitude, are now separately evaluated.

To establish the effect of Acceleration Number on the excess temperature, Cases D-1 (Ac=0.13), and D-2 (Ac=0.26) with a Re=6835, and Cases D-3 (Ac=0.26) and D-7 (Ac=6.44) with a Re=3417 are examined. At Re=6835, Acceleration Number has mainly contributed to an increase in excess temperature deviations except for PJ8 at SC=45 °C and MW145 at SC=10 °C. At the lower Reynolds No of 3417, however, Acceleration Number has a decreasing effect on the excess temperature deviations except for Case PJ10 at $v = 75$ ml/min and SC=45°C, Case PJ8 data at SC=45 °C, and Case MW145 at SC= 10°C. This means that at Re=6835, the increasing effect of Acceleration Number on the excess temperature deviations is valid for 75% of dynamic cases, whereas for Re=3417 Acceleration Number has less impact on the temperature differences for 63% of data cases. It appears that the temperature differences with Acceleration Number is nonlinear, and therefore, other parameters are needed to understand the effects of vibration on excess temperature.

To study the Reynolds Number effect, Cases D-2 (Re=6835) and D-3 (Re=3417) are compared. Table 8 for PJ8, shows that by increasing the Reynolds Number the deviations for both subcooling degrees are decreased while the temperature differences for MW145 are all increased. In other words, it can be deduced that at the highest volumetric spray flux (9.03×10^{-3}m^{3}s^{-1}/m^2 for MW145), Reynolds number increases the temperature deviations (which is a negative thing for thermal management purposes). And at the lowest volumetric flux of 0.77×10^{-3}m^{3}s^{-1}/m^2 for PJ8, increasing Reynolds Number decreases these temperature deviations (which is a positive thing for thermal management systems). The PJ10 nozzle (which has volumetric fluxes of 1.05 $\times10^{-3}$ and 1.40 $\times10^{-3}$ m^{3}s^{-1}/m^2 corresponding to 75ml/min and 100ml/min respectively) appears to be at the transition between these two increasing and decreasing effects of Reynolds Number. For the lower volumetric flux of 1.05 $\times10^{-3}$ m^{3}s^{-1}/m^2 which is closer to that for the PJ8 (the decreasing effect of Reynolds Number is only recognised for the PJ10 at SC=10 °C). For the volumetric flux of 1.40 $\times10^{-3}$ m^{3}s^{-1}/m^2 (which is about twice that of the PJ8, and therefore closer to the MW145 volumetric flux) the increasing effect of Reynolds number on the temperature differences is detectable at both subcooling degrees (given in Table 8), an effect mentioned earlier for the MW145 nozzle. The only exception is for PJ10 nozzle at the lower volumetric flux of 1.05 $\times10^{-3}$ m^{3}s^{-1}/m^2 (75 ml/min in Table 8) and SC=45 °C which stems from the dominant effect of subcooling on different heat transfer mechanisms of spray cooling.

To investigate the effect of amplitude, Cases D-4 (a=1mm) and D-5 (a=0.2mm), at a frequency of 50Hz, are examined. For PJ nozzles, all the temperature differences except for PJ8 at SC=45 °C have been decreased by augmenting the amplitude. For the MW145 and PJ8 at SC=45 °C, this behaviour is the exact opposite from that previously observed. As far as establishing the influence of frequency, Cases D-5 (50Hz) and D-6 (100Hz) with the same amplitude of 0.2 mm, are good candidates. For all nozzles at SC=45 °C, doubling the frequency increases the maximum temperature differences. For SC=10 °C, it seems that volumetric flux has again been the governing effect on the excess temperature deviations. Starting with the PJ8 nozzle ($\bar{v}'' = 0.77\times10^{-3}$m^{3}s^{-1}/m^2) and the PJ10 ($\bar{v}'' = 1.05\times10^{-3}$m^{3}s^{-1}/m^2), doubling the frequency decreases the temperature deviations, while $\bar{v}'' = 1.40\times10^{-3}$m^{3}s^{-1}/m^2 (for the PJ10), appears to be a transition point above which, doubling the frequency starts to increase the temperature difference. The increasing effect of frequency on maximum temperature also remains valid with a lower intensity for the MW145 nozzle with $\bar{v}'' = 9.03\times10^{-3}$m^{3}s^{-1}/m^2.

Having used the measured data obtained from the experimental test rig discussed in Section 3 to show the nonlinear dependence of the CHF and its associated temperature for different of nozzle types, it is now appropriate to consider the use of the correlation models discussed in Section 2 in creating a prediction capability. This is now a question of appropriately calibrating the dynamic correlation model Eq. (2) in the dynamic form given in Table 3 using the dynamic Boiling Number Eq. (4).

6. Calibrating a dynamic correlation model for CHF and associated temperature prediction

To calibrate an appropriate dynamic correlation model in Table 3 for CHF and associated temperature prediction, a nonlinear least square regression is used. This fitting process is also used to calibrate 'static' correlations from Table 3, which are used for comparative purposes. The Matlab Levenberg-Marquardt optimisation algorithm is used (with the method option set to 'bisquare' for robustness). The PJ8 and PJ10 nozzles are used to construct both static and dynamic functional correlational models.

Table 9 shows the parameters obtained in calibrating both the dynamic and static models which are those obtained which minimise the RMS errors between the prediction and measured data for the PJ and MW145 nozzles. The parameter values themselves obtained for the calibrated models shown in Table 9 qualitatively support the finding discussed in Section 4 for each nozzle. For example, the parameter 'a' for the MW145 nozzle is greater than those for PJ nozzles in both dynamic and static cases indicating that MW145 correlation model will obtain a higher CHF prediction. Negative values for parameter b also support the inverse behaviour of MW145 in response to subcooling degrees.

Fig. 12 shows a correlation diagram for PJ and MW145 nozzles giving the predicted CHF values using the dynamic and static

Table 9
Dynamic and static correlation parameters for the PJ and MW145 nozzles.

Dynamic correlation model $Bo = a\,Ja^b\left(\frac{\rho_l^2\sigma v}{\mu_l{}^3}\right)^c Re_V^d\left(\frac{a}{H}\right)^e Ac^f$, **Parameters: a, b, c, d, e, f**

Static correlation model $Bo = a\,Ja^b\left(\frac{\rho_l^2\sigma v}{\mu_l{}^3}\right)^c$, **Parameters: a, b, c**

Correlation	Nozzles	Parameters					
		a	b	c	d	e	f
Dynamic	PJ8 and PJ10	2.46E-04	0.0497	0.7348	-0.4958	0.2357	0.2329
	MW145	3.43E-04	-0.0317	0.7512	-0.4535	0.2065	0.1886
Static	PJ8 and PJ10	1.71E-06	0.0507	0.7383			
	MW145	2.81E-05	-0.0681	0.6565			

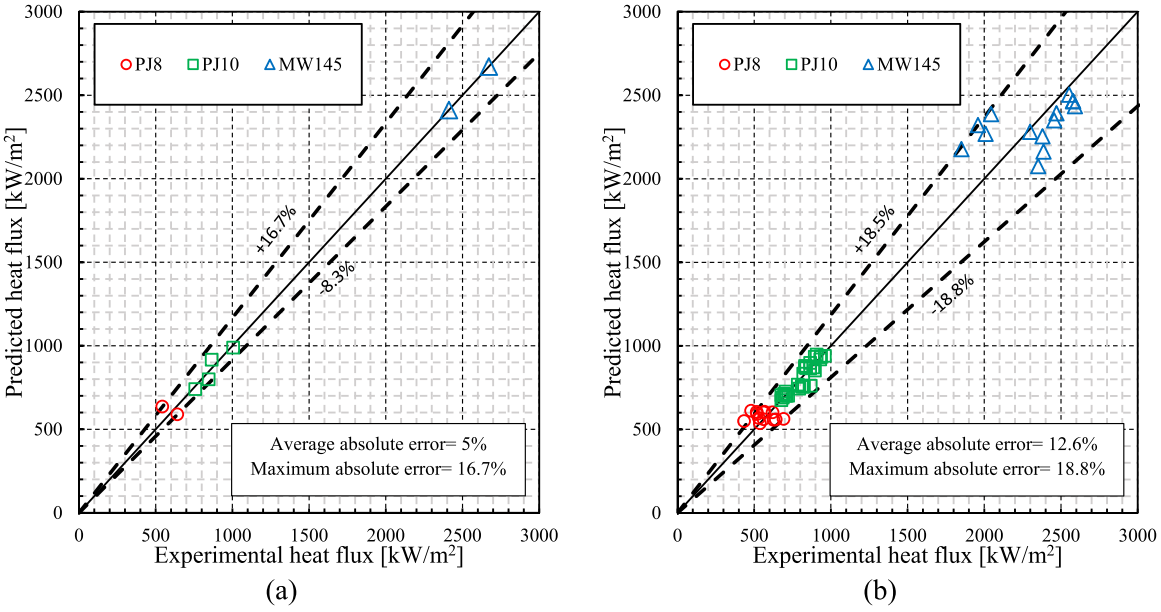

Fig. 12. Correlation of CHF predictions using the models in Table 9 versus experimental measurement showing error bands: (a) *static* and (b) *Dynamic.*

models and parameters in Table 9 (vertical axis), compared to the experimentally-measured CHF values (using the horizontal axis). Model error bands are also shown plus numerical values of the average and maximum absolute errors. Fig. 12a shows the static correlation results also showing error bands of 0%, -8.3%, and +16.7%. A total of 8 data points are predicted having an average absolute error of 5%, and a maximum absolute error of 16.7%. The accuracy of the predicted (static) CHF results are comparable with those for other static models in the literature (See Table 1) the quality of which is deemed to be good. The dynamic model prediction is shown in Fig. 12b plus error bands of 0%, -18.8% and +18.5%. The average and maximum absolute deviations of the predictions are respectively 12.6% and 18.8%. The most accurate predictions are obtained for the PJ10 nozzle. By contrast, the maximum absolute errors are for the PJ8 nozzle for the static case with SC=45 °C, and for dynamic case of D-7 (which is at high frequency vibration). This accuracy partly stems from the higher number of PJ10 data points (28 for PJ10, 14 for MW145, and 12 for PJ8), consequently better resolution from the PJ10 data.

6.1. Excess temperature correlation model

For the purpose of thermal management, there is also a need to use a correlation model to predict the excess temperature at which CHF occurs (which is also known as maximum controllable surface temperature or stable CHF temperature). Mudawar and Valentine [30] determined T_{max} by combining a CHF model with a different functional form which included the excess temperature ($\Delta T_{excess} = T_{w,max} - T_{sat}$) and then solving for the surface temperature. The functional form containing excess temperature when based on generalized Π–Theorem (Section 2) takes the form:

$$\frac{\Delta T_{excess}}{\Delta T_{Sub}} = a\left(\frac{q_{CH}H}{\mu_l h_{fg}}\right)^b\left(\frac{\rho_l^2\sigma v}{\mu_l{}^3}\right)^c Re_V^d\left(\frac{a}{H}\right)^e Ac^f \tag{7}$$

where the critical heat flux, q_{CH}, in Eq. (7) is obtained from fitted dynamic correlation model in Table 9. This requires Eq. (7) to be used with the previously fitted correlation model for CHF. Therefore Eq. (7) is separately fitted to measured CHF and excess temperature data points associated with both the PJ and MW145 nozzles. In Eq. (7), a dimensionless surface temperature ($T_{CHF} = \Delta T_{excess}/\Delta T_{Sub}$) is defined similar to the CHF studies of Dou et al [31] and Abbasi and Kim [59].

To achieve high accuracy in fitting Eq. (7), the data is split into two different subcooling degrees. The reason for this is the high dependency of the excess temperature on subcooling degrees (as indicated by the trends identified earlier). The fitted parameters with the least rms errors are given in Table 10. Fig. 13 shows the predicted excess temperature compared with the experimentally measured values for two different subcooling degrees of 10 °C (Fig. 12a) and 45 °C (Fig. 13b). The error bands for SC=10°C have a wider range (-15.5% and +15.9%) than those for SC=45°C (-9.8% and +10.3%) indicating the effect of subcooling on the excess temperature. As expected, at SC=10 °C, the PJ10 nozzle results deviate more than the PJ8 excess temperature in comparison to what can be seen for the PJ10 and PJ8 data at SC=45 °C. When an evaporative spray cooling thermal management system requires the predicted maximum controllable temperature to safely set boundaries

Table 10
Excess temperature correlation parameters for PJ and MW145 nozzles at two subcooling degrees.

Excess temperature correlation model $\frac{\Delta T_{excess}}{\Delta T_{Sub}} = \alpha\left(\frac{q_{CH}H}{\mu_l h_{fg}}\right)^{\beta}\left(\frac{\rho_l^2 \sigma v}{\mu_l^3}\right)^{\gamma} Re_V^{\delta}\left(\frac{a}{H}\right)^{\varepsilon} Ac$
Parameters: $\alpha\ \beta\ \gamma\ \delta\ \varepsilon\ \varepsilon$

Subcooling (°C)	Nozzles	Parameters					
		α	β	γ	δ	ε	ε
10	PJ8 and PJ10	1.22E-05	-0.2879	0.6472	-0.0783	0.0074	-0.0011
	MW145	1.26E-05	0.1644	0.6112	-0.0738	-0.0479	-0.0664
45	PJ8 and PJ10	1.28E-04	-0.2393	0.3228	0.2411	-0.1228	-0.1302
	MW145	3.46E-05	1.1914	0.2584	0.1030	-0.0607	-0.0466

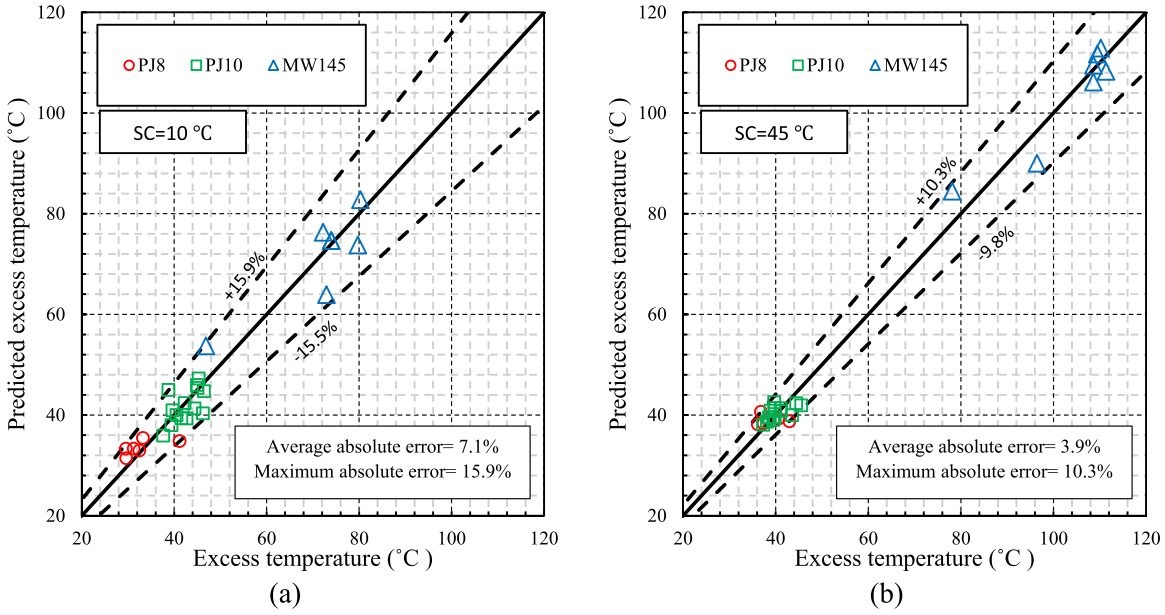

Fig. 13. Excess temperature predicted by the correlation model in Table 10 showing error bands: (a) SC=10 °C and (b) SC=45 °C.

for controller operation, the model prediction quality is reasonable for both subcooling degrees.

7. Conclusions

Experimental measurements have been obtained to investigate the effect of vibrating surfaces on the critical heat flux (CHF) in spray evaporative cooling and to assess the effectiveness of calibrated prediction models. Prediction models have been constructed using dimensional analysis, to take account of key dynamic parameters. Experimental hardware has been purpose-designed to electrically-heat a flat copper test-piece, located inside a spray-chamber mounted on top of a shaker, which has been used to generate data. A range of appropriately large-amplitude and high-frequency test-piece surface vibrations have been examined involving spray evaporative cooling. Three nozzle types, using distilled water have been examined, namely a PJ8, PJ10, and MW145 nozzle with respective flow rates of 75 ml/min, 100 ml/min, and 55 ml/min. CHF data points, and their corresponding excess temperatures, have been obtained for two 'subcooling degrees' of 10°C and 45°C. All the key vibrational effects have also been expressed in terms of non-dimensional parameters.

For the static experiments, without vibration, the effect of flow rate, volumetric flux, and subcooling have been found to be largely in agreement with the published literature. For the dynamic cases, the effect of vibration is best explained in terms of nondimensional Vibrational Reynolds Number and Acceleration Number. With vibrating surfaces, increasing volumetric flux, is found to enhance CHF. For the PJ10 nozzle, Acceleration Number has the largest influence for both flow rate and subcooling degrees, where the deteriorating effect of vibration becomes evident for increasing subcooling degrees. By contrast, for the low flow-rate nozzles of the PJ8 and MW145, the impeding effect of vibration reduces with increasing subcooling. For both flow-rate and subcooling degrees of the PJ nozzles, increasing Reynolds Number initially enhances CHF but then impedes it. This is also found to be true for the MW145 nozzle (at SC=10°C) but at SC=45°C the opposite effect occurs owing to the high dependency of MW145 nozzle on the subcooling effect. For PJ nozzles, Acceleration had an enhancing effect.

The effect of vibration on excess temperature showed that for all nozzle types, high-frequency vibration produces significant deviations, although for the MW145 nozzle at SC= 45°C, vibration amplitude had more effect. In general, the volumetric flux was found to produce the greatest influence on excess temperature.

Predictions of CHF, and associated excess temperature, using calibrated correlation models for the dynamic conditions, were very reasonable, with maximum absolute errors of 18.8% and 15.9%, respectively. These calibrated correlation models are of potential value for safe operation of thermal management systems using spray evaporative cooling.

Declaration of Competing Interest

The authors confirm that there is no conflict of interest associated with this manuscript.

Acknowledgements

The authors acknowledge support for the development of the experimental facilities, in terms of funding from the EPSRC (under Contract Number: EP/M005755/1), and technical support from Ford Dunton UK, Ford Dearborn USA, Denso Italy, and the Ricardo Technical Centre Shoreham UK. The authors also wish to acknowledge additional financial and technical support from the Ricardo Shoreham Technical Centre, UK.

References

[1] S. Somasundaram, A.A. Tay, An experimental study of closed loop intermittent spray cooling of ICs, Applied thermal engineering 31 (14-15) (2011) 2321–2331.
[2] G. Liang, I. Mudawar, Review of spray cooling–Part 2: High temperature boiling regimes and quenching applications, International Journal of Heat Mass Transfer 115 (2017) 1206–1222.
[3] Y. Ding, Z.P. Cano, A. Yu, J. Lu, Z. Chen, Automotive Li-ion batteries: current status and future perspectives, Electrochemical Energy Reviews 2 (1) (2019) 1–28.
[4] S. Khandekar, G. Sahu, K. Muralidhar, E.Y. Gatapova, O.A. Kabov, R. Hu, X. Luo, L. Zhao, Cooling of High-Power LEDs by Liquid Sprays: Challenges and Prospects, Applied Thermal Engineering (2020) 115640.
[5] J. Wang, Y. Li, J. Wang, Transient performance and intelligent combination control of a novel spray cooling loop system, Chinese Journal of Aeronautics 26 (5) (2013) 1173–1181.
[6] Y. Ding, Y. Li, Y. Li, W. Chen, H. Zhang, D. Li, Intensive cooling method for power electronic component with high heat flux, in: 2014 13th International Conference on Control Automation Robotics & Vision (ICARCV), IEEE, 2014, pp. 163–168.
[7] J.-X. Wang, W. Guo, K. Xiong, S.-N. Wang, Review of aerospace-oriented spray cooling technology, Progress in Aerospace Sciences 116 (2020) 100635.
[8] Y. Yang, L. Yang, X. Du, Y.J.A.T.E. Yang, Pre-cooling of air by water spray evaporation to improve thermal performance of lithium battery pack 163 (2019) 114401.
[9] S. Lei, Y. Shi, G. Chen, Heat-pipe based spray-cooling thermal management system for lithium-ion battery: Experimental study and optimization, International Journal of Heat and Mass Transfer 163 (2020) 120494.
[10] T. Sai, K. Reddy, Design of fuzzy gain scheduler for superheater temperature control in power plant, in: 2016 2nd International Conference on Control, Instrumentation, Energy & Communication (CIEC), IEEE, 2016, pp. 521–525.
[11] J. Zhang, T.S. Fisher, P.V. Ramachandran, J.P. Gore, I. Mudawar, A review of heat transfer issues in hydrogen storage technologies, JOURNAL OF HEAT TRANSFER (2005) ASME.
[12] O.V. Kartuzova, M. Kassemi, J.P. Moder, J.H. Agui, Self-pressurization and spray cooling simulations of the multipurpose hydrogen test bed (MHTB) ground-based experiment, in: 50th AIAA/ASME/SAE/ASEE Joint Propulsion Conference, 2014, p. 3578.
[13] R.B. Biniwale, N. Kariya, H. Yamashiro, M. Ichikawa, Heat transfer and thermographic analysis of catalyst surface during multiphase phenomena under spray-pulsed conditions for dehydrogenation of cyclohexane over Pt catalysts, The Journal of Physical Chemistry B 110 (7) (2006) 3189–3196.
[14] J. Gibbins, H. Chalmers, Carbon capture and storage, Energy policy 36 (12) (2008) 4317–4322.
[15] The ten point plan for a green industrial revolution, in: E.I.S. Department for Business, Prime Minister's Office, 10 Downing Street, The Rt Hon Alok Sharma MP, and The Rt Hon Boris Johnson MP (Ed.), https://www.gov.uk/government/publications/the-ten-point-plan-for-a-green-industrial-revolution, 2020.
[16] J. Breitenbach, I.V. Roisman, C.J.E.i.F. Tropea, From drop impact physics to spray cooling models: a critical review 59 (3) (2018) 55.
[17] H. Liu, C. Cai, M. Jia, J. Gao, H. Yin, H. Chen, Experimental investigation on spray cooling with low-alcohol additives, Applied Thermal Engineering 146 (2019) 921–930.
[18] G. Liang, I. Mudawar, Review of spray cooling–Part 1: Single-phase and nucleate boiling regimes, and critical heat flux, International Journal of Heat and Mass Transfer 115 (2017) 1174–1205.
[19] V. Terekhov, P. Karpov, A. Nazarov, A. Serov, Unsteady heat transfer at impinging of a single spray pulse with various durations, International Journal of Heat and Mass Transfer 158 (2020) 120057.
[20] M.R. Panão, A.L. Moreira, Intermittent spray cooling: a new technology for controlling surface temperature, International Journal of Heat Fluid Flow 30 (1) (2009) 117–130.
[21] X. Zhao, B. Zhang, X. Xi, Z. Yin, Analysis and prediction of single-phase and two-phase cooling characteristics of intermittent sprays, International Journal of Heat Mass Transfer 133 (2019) 619–630.
[22] M. Panão, A. Moreira, Thermo-and fluid dynamics characterization of spray cooling with pulsed sprays, Experimental Thermal and Fluid Science 30 (2) (2005) 79–96.
[23] A. Moreira, M. Panao, Heat transfer at multiple-intermittent impacts of a hollow cone spray, International Journal of Heat and Mass Transfer 49 (21-22) (2006) 4132–4151.
[24] M.R. Panão, A.L. Moreira, Two-phase cooling characteristics of a multiple-intermittent spray, 13th International Symposium on Applications of Laser Techniques to Fluid Mechanics, 26th-29th June, Citeseer, 2006.
[25] A.L. Moreira, J. Carvalho, M.R. Panao, An experimental methodology to quantify the spray cooling event at intermittent spray impact, International Journal of Heat and Fluid Flow 28 (2) (2007) 191–202.
[26] M.R. Panão, A.L. Moreira, Intermittent spray cooling: a new technology for controlling surface temperature, International Journal of Heat and Fluid Flow 30 (1) (2009) 117–130.
[27] M.R. Panão, A.M. Correia, A.L. Moreira, High-power electronics thermal management with intermittent multijet sprays, Applied thermal engineering 37 (2012) 293–301.
[28] S. Somasundaram, A.A. Tay, Intermittent spray cooling—Solution to optimize spray cooling, in: 2012 IEEE 14th Electronics Packaging Technology Conference (EPTC), IEEE, 2012, pp. 588–593.
[29] B. Majaron, L.O. Svaasand, G. Aguilar, J.S. Nelson, Intermittent cryogen spray cooling for optimal heat extraction during dermatologic laser treatment, Physics in Medicine & Biology 47 (18) (2002) 3275.
[30] I. Mudawar, W. Valentine, Determination of the local quench curve for spray–cooled metallic surfaces, Journal of Heat Treating 7 (2) (1989) 107–121.
[31] R. Dou, Z. Wen, G. Zhou, Heat transfer characteristics of water spray impinging on high temperature stainless steel plate with finite thickness, International Journal of Heat and Mass Transfer 90 (2015) 376–387.
[32] K. Baysinger, K. Yerkes, R. Harris, T. Michalak, J. McQuillen, Design of a microgravity spray cooling experiment, in: 42nd AIAA Aerospace Sciences Meeting and Exhibit, 2004, p. 966.
[33] S.K. Mishra, A. Arora, H. Chandra, Application of Vibration on Heat Transfer-A Review, J i-Manager's Journal on Future Engineering Technology 15 (1) (2019) 72.
[34] J. Kim, J. Oh, H. Lee, Review on battery thermal management system for electric vehicles, Applied thermal engineering 149 (2019) 192–212.
[35] S. Jafari, T. Nikolaidis, Thermal management systems for civil aircraft engines: Review, challenges and exploring the future, Applied Sciences 8 (11) (2018) 2044.
[36] J. Doty, K. Yerkes, L. Byrd, J. Murthy, A. Alleyne, M. Wolff, S. Heister, T. Fisher, Dynamic thermal management for aerospace technology: review and outlook, Journal of Thermophysics Heat Transfer 31 (1) (2017) 86–98.
[37] H. Atashi, A. Alaei, M. Kafshgari, R. Aeinehvand, S. Rahimi, New Pool Boiling Heat Transfer in the Presence of Low-Frequency Vibrations Into a Vertical Cylindrical Heat Source, Experimental Heat Transfer 27 (5) (2014) 428–437.
[38] J.T. Jose, J. Dunne, Numerical Simulation of Single-Droplet Dynamics, Vaporization, and Heat Transfer from Impingement onto Static and Vibrating Surfaces, J Fluids 5 (4) (2020) 188.
[39] Z. Wang, Y. Xing, X. Liu, L. Zhao, Y. Ji, Computer modeling of droplets impact on heat transfer during spray cooling under vibration environment, Applied Thermal Engineering 107 (2016) 453–462.
[40] A. Sarmadian, J. Dunne, C. Long, J.T. Jose, J.-P. Pirault, C. Rouaud, Heat flux correlation models for spray evaporative cooling of vibrating surfaces in the nucleate boiling region, International Journal of Heat Mass Transfer 160 (2020) 120159.
[41] A. Sathyabhama, S. Prashanth, Enhancement of boiling heat transfer using surface vibration, Heat Transfer—Asian Research 46 (1) (2017) 49–60.
[42] L. Elston, K. Yerkes, S. Thomas, J. McQuillen, Effect of Variable Gravity on the Cooling Performance of a 16-Nozzle Spray Array, in: 47th AIAA Aerospace Sciences Meeting Including The New Horizons Forum and Aerospace Exposition, 2009, p. 1025.
[43] L.J. Elston, K.L. Yerkes, S.K. Thomas, J. McQuillen, Cooling performance of a 16-nozzle array in variable gravity, Journal of thermophysics heat transfer 23 (3) (2009) 571–581.
[44] T.E. Michalak, K.L. Yerkes, S.K. Thomas, J.B. McQuillen, Acceleration effects on the cooling performance of a partially confined FC-72 spray, Journal of Thermophysics Heat Transfer 24 (3) (2010) 463–479.
[45] G. Bluman, Dimensional analysis, modelling and symmetry, International Journal of Mathematical Education in Science and Technology 14 (3) (1983) 259–272.
[46] A.A. Sonin, A generalization of the Π-theorem and dimensional analysis, Proceedings of the National Academy of Sciences 101 (23) (2004) 8525–8526.
[47] E. Buckingham, Model experiments and the forms of empirical equations, Verlag nicht ermittelbar, 1915.
[48] E. Buckingham, On physically similar systems; illustrations of the use of dimensional equations, Physical review 4 (4) (1914) 345.
[49] K.A. Estes, I. Mudawar, Correlation of Sauter mean diameter and critical heat flux for spray cooling of small surfaces, International Journal of Heat and Mass Transfer 38 (16) (1995) 2985–2996.
[50] I. Mudawar, K. Estes, Optimizing and predicting CHF in spray cooling of a square surface, Journal of Heat Transfer 118 (1996) 672–679.
[51] S. Jiang, V.K. Dhir, Spray cooling in a closed system with different fractions of non-condensibles in the environment, International journal of heat and mass transfer 47 (25) (2004) 5391–5406.
[52] S.J. Thiagarajan, S. Narumanchi, R. Yang, Effect of flow rate and subcooling on spray heat transfer on microporous copper surfaces, International Journal of Heat and Mass Transfer 69 (2014) 493–505.
[53] M. Visaria, I. Mudawar, Effects of high subcooling on two-phase spray cooling and critical heat flux, International journal of heat and mass transfer 51 (21-22) (2008) 5269–5278.
[54] M.S. Sehmbey, L.C. Chow, O.J. Hahn, M.R. Pais, Effect of spray characteristics on

spray cooling with liquid nitrogen, Journal of Thermophysics and heat Transfer 9 (4) (1995) 757–765.
[55] L. Chow, M. Sehmbey, M. Pais, Critical heat flux in spray cooling, in: 34th Aerospace Sciences Meeting and Exhibit, 1996, p. 727.
[56] M. Sawyer, S. Jeter, S. Abdel-Khalik, A critical heat flux correlation for droplet impact cooling, International Journal of Heat and Mass Transfer 40 (9) (1997) 2123–2131.
[57] E.A. Silk, J. Kim, K. Kiger, Energy conservation based spray cooling CHF correlation for flat surface small area heaters, in: ASME/JSME 2007 Thermal Engineering Heat Transfer Summer Conference collocated with the ASME 2007 InterPACK Conference, American Society of Mechanical Engineers, 2007, pp. 805–813.
[58] E. Cabrera, Heat flux correlation for spray cooling in the nucleate boiling regime, Experimental heat transfer 16 (1) (2003) 19–44.
[59] B. Abbasi, J. Kim, Prediction of PF-5060 spray cooling heat transfer and critical heat flux, Journal of heat transfer 133 (10) (2011) 101504.
[60] X. Zhao, B. Zhang, X. Xi, Z. Yin, Analysis and prediction of single-phase and two-phase cooling characteristics of intermittent sprays, International Journal of Heat and Mass Transfer 133 (2019) 619–630.
[61] R.-H. Chen, L.C. Chow, J.E. Navedo, Optimal spray characteristics in water spray cooling, International Journal of Heat Mass Transfer 47 (23) (2004) 5095–5099.
[62] S. Toda, A study of mist cooling (1st report, investigation of mist cooling), J Kikaigakkai Ronbunshu 38 (1972) 581–588.
[63] S. Toda, A study of mist cooling (2nd report: theory of mist cooling and its fundamental experiments), Heat Transf.-Jap. Res 3 (1974) 1–44.
[64] K. Baumeister, F. Simon, Leidenfrost temperature—its correlation for liquid metals, cryogens, hydrocarbons, and water, Transactions of ASME, Journal of Heat Transfer (1973).
[65] R.J. Moffat, Describing the uncertainties in experimental results, Experimental thermal and fluid science 1 (1) (1988) 3–17.
[66] S. Toda, H. Uchida, Study of liquid film cooling with evaporation and boiling, J Trans. JSME 2 (1973) 44–62.
[67] Y. Hou, J. Liu, X. Su, Y. Qian, L. Liu, X. Liu, Experimental study on the characteristics of a closed loop R134-a spray cooling, Experimental Thermal and Fluid Science 61 (2015) 194–200.
[68] L.C. Chow, M.S. Sehmbey, M.R. Pais, High heat flux spray cooling, Annual Review of Heat Transfer 8 (1997).
[69] G. Moreno Jr, S.M. You, E. Steinthorsson, Spray cooling performance of single and multi-jet spray nozzles using subcooled FC-72, in: Heat Transfer Summer Conference, 2007, pp. 783–790.
[70] M. Pais, L. Chow, E. Mahefkey, Surface roughness and its effects on the heat transfer mechanism in spray cooling, J. Heat Transf. – Trans. ASME 114 (1992) 211–219.
[71] R.-H. Chen, L.C. Chow, J.E. Navedo, Effects of spray characteristics on critical heat flux in subcooled water spray cooling, International Journal of Heat and Mass Transfer 45 (19) (2002) 4033–4043.
[72] D.E. Tilton, Spray cooling PhD Dissertation, University of Kentucky, Lexington, USA, 1989.
[73] L. Lin, R. Ponnappan, Critical heat flux of multi-nozzle spray cooling, J. Heat Transfer - Trans. ASME 126 (3) (2004) 482–485.
[74] M. Monde, Critical heat flux in the saturated forced convection boiling on a heated disk with impinging droplets, Trans. JSME (1980) 849–858.
[75] I. Mudawar, K. Estes, Optimizing and predicting CHF in spray cooling of a square surface, Journal of Heat Transfer 118 (3) (1996) 672–679.
[76] M. Visaria, I. Mudawar, Effects of high subcooling on two-phase spray cooling and critical heat flux, International journal of heat mass transfer 51 (21-22) (2008) 5269–5278.
[77] Y. Zhang, L. Pang, Y. Xie, S. Jin, M. Liu, Y. Ji, Experimental investigation of spray cooling heat transfer on straight fin surface under acceleration conditions, Experimental Heat Transfer 28 (6) (2015) 564–579.
[78] Y. Zhang, L. Pang, M. Liu, Y. Xie, Investigation of spray cooling: Effect of different heater surfaces under acceleration, International Communications in Heat Mass Transfer 75 (2016) 223–231.
[79] B.L. Conrad, J.C. Springmann, L.A. McGill, T.A. Shedd, Effectiveness of linear spray cooling in microgravity, in: AIP Conference Proceedings, American Institute of Physics, 2009, pp. 67–72.